

# A New Norm for Seasonal Sea Ice Advance Predictability in the Chukchi Sea: Rising Influence of Ocean Heat Advection

TAKUYA NAKANOWATARI,<sup>a</sup> JUN INOUE,<sup>b</sup> JINLUN ZHANG,<sup>c</sup> EIJI WATANABE,<sup>d</sup> AND HIROSHI KURODA<sup>a</sup>

<sup>a</sup> Fisheries Resources Institute, Japan Fisheries Research and Education Agency, Kushiro, Japan

<sup>b</sup> National Institute of Polar Research, Tachikawa, Japan

<sup>c</sup> Polar Science Center, Applied Physics Laboratory, University of Washington, Seattle, Washington

<sup>d</sup> Institute of Arctic Climate and Environment Research, JAMSTEC, Yokosuka, Japan

(Manuscript received 1 June 2021, in final form 13 January 2022)

**ABSTRACT:** Predictability of seasonal sea ice advance in the Chukchi Sea has been investigated in the context of ocean heat transport from the Bering Strait; however, the underlying physical processes have yet to be fully clarified. Using the Pan-Arctic Ice–Ocean Modeling and Assimilation System (PIOMAS) reanalysis product (1979–2016), we examined seasonal predictability of sea ice advance in early winter (November–December) and its source using canonical correlation analysis. It was found that 2-month leading (September–October) surface heat flux and ocean heat advection is the major predictor for interannual variability of sea ice advance. Surface heat flux is related to the atmospheric cooling process, which has influenced sea ice area in the southeastern Chukchi Sea particularly in the 1980s and 1990s. Anomalous surface heat flux is induced by strong northeasterly winds related to the east Pacific/North Pacific teleconnection pattern. Ocean heat advection, which is related to fluctuation of volume transport in the Bering Strait, leads to decrease in the sea ice area in the northwestern Chukchi Sea. Diagnostic analysis revealed that interannual variability of the Bering Strait volume transport is governed by arrested topographic waves (ATWs) forced by southeasterly wind stress along the shelf of the East Siberian Sea. The contribution of ocean heat flux to sea ice advance has increased since the 2000s; therefore, it is suggested that the major factor influencing interannual variability of sea ice advance in early winter has shifted from atmospheric cooling to ocean heat advection processes.

**SIGNIFICANCE STATEMENT:** Predictability of sea ice advance in the marginal Arctic seas in early winter is a crucial issue regarding future projections of the midlatitude winter climate and marine ecosystem. This study examined seasonal predictability of sea ice advance in the Chukchi Sea in early winter using a statistical technique and historical model simulation data. We identified that atmospheric cooling and ocean heat transport are the two main predictors of sea ice advance, and that the impact of the latter has become amplified since the 2000s. Our new finding suggests that the precise information on wind-driven ocean currents and temperatures is crucial for the skillful prediction of interannual variability of sea ice advance under present and future climatic regimes.


**KEYWORDS:** Arctic; Sea ice; Atmosphere-ocean interaction; Ocean dynamics; Statistical forecasting; Climate variability

## 1. Introduction

The Chukchi Sea is a high-latitude seasonally ice-covered shelf sea in the Pacific Arctic region and directly affected by substantial heat (Woodgate et al. 2010) and freshwater (Serreze et al. 2006) transport from the Bering Strait. In the western Chukchi Sea, large amounts of nutrients are carried by northward-flowing water through the Anadyr Strait where coastal upwelling occurs (Kawaguchi et al. 2020), sustaining high phytoplankton productivity and a substantial amount of biomass (Springer and McRoy 1993). The marine ecosystem in this region is characterized by a large volume of benthic biomass in the cold-water environment, whereby the high

primary production at the surface is not effectively consumed by zooplanktons (Hunt et al. 2013). Recently, it was reported that the period of sea ice coverage in the Chukchi Sea has become shortened by 80 days since 1979 (Serreze et al. 2016). A shortened period of sea ice coverage and the resultant increase in ocean temperature reduces the habitat for marine benthos; consequently, a northward shift of the pelagic–benthic ecosystem is occurring (Grebmeier et al. 2006).

Sea ice coverage has an insulating effect regarding surface heat flux from the ocean to the atmosphere, and the reduction of wintertime sea ice area in the marginal sea ice zone of the Arctic Ocean increases this surface heat flux (e.g., Smedsrud et al. 2013), which in turn acts as a driving force of the atmosphere. This anomalous surface heat flux is considered one of the possible causes of the severe wintertime climate in the midlatitudes (e.g., Overland 2020). On the basis of observational analyses and climate model simulations, Kug et al. (2015) highlighted that occurrence of severe winters over North America has increased since the 1990s because of anomalous warming in the East Siberian–Chukchi Sea region.

 Denotes content that is immediately available upon publication as open access.

Corresponding author: Takuya Nakanowatari, nakanowatari@takuya@affrc.go.jp

DOI: 10.1175/JCLI-D-21-0425.1

© 2022 American Meteorological Society. For information regarding reuse of this content and general copyright information, consult the AMS Copyright Policy (www.ametsoc.org/PUBSReuseLicenses).

Ensemble experiments with an atmospheric general circulation model prescribed with sea ice loss indicate that the anomalous atmospheric circulation responsible for severe winters over the North America is induced by a low sea ice area (SIA) in the Bering Sea (Lee et al. 2015; Screen 2017). A recent study reported that a low sea ice anomaly north of the Bering Strait in late autumn was responsible for the cold winter in 2017/18 over eastern Eurasia, including the North Pacific Ocean, via the large southward jet stream pathways formed over Asia and America (Tachibana et al. 2019). Kuroda et al. (2020) showed that SST in the western part of the North Pacific subtropical gyre gradually decreased during 2000–10, and they discussed the linkage between severe winters in Eurasia and the cold regime of ocean temperature, which has potentially affected major commercial fishery resources (e.g., Japanese sardines).

In contrast to these climatic consequences and problems for the marine ecosystem, sea ice reduction in the Chukchi Sea also has potential impact on the possibility of shorter shipping routes for commercial vessels. Use of trans-Arctic shipping routes is estimated to reduce the navigation distance between Europe and Asia regions by approximately 40% in comparison with routes via the Suez Canal (Schøyen and Bråthen 2011). Automatic Identification System tracking data show that the number of commercial vessels has already increased in summertime in the Arctic Ocean (Eguíluz et al. 2016). The search for the optimal Northern Sea Route is conducted using atmospheric and oceanic environmental information (Koyama et al. 2021). According to future projections of climate model simulations under global warming scenarios, the duration of the Arctic navigation season is expected to increase by 4–8 months by the mid–late twenty-first century and also the possibility of open water vessel navigation (Melia et al. 2016; Chen et al. 2020). Thus, predictability of sea ice conditions in the Chukchi Sea is important both for planning economic and safe navigation and for future projections of the marine ecosystem and fishery resources in the North Pacific.

Wintertime SIA variability in the Bering Sea has been studied by many researchers in terms of large-scale atmospheric wind conditions (e.g., Sasaki and Minobe 2005), cyclone activity (Overland and Pease 1982), local winds and ice influx from the Arctic Ocean (Zhang et al. 2010), and ocean heat advected from the Pacific Ocean (Nakanowatari et al. 2015), but few studies have specifically investigated the Chukchi Sea in early winter. Serreze et al. (2016) examined the interannual variability of sea ice retreat and advance in the Chukchi Sea on the basis of long-term (30 yr) observations. They found that the starting date of sea ice advance is correlated significantly with summertime Bering Strait heat inflow. Following analysis of mooring observations, Serreze et al. (2019) reported that the largest heat transport through the Bering Strait was recorded in October 2016, and they discussed the importance of warm water temperature and the wind conditions driving the Bering Strait volume transport. A medium-range sea ice forecast experiment demonstrated that having reliable initial conditions of water temperature in the Bering

Sea improves forecasts of wintertime sea ice in the Chukchi Sea (De Silva et al. 2020).

Although the importance of ocean heat conditions regarding sea ice variability in the Chukchi Sea has been examined by several researchers (e.g., Serreze et al. 2019; Lenetsky and Serreze 2021; Lenetsky et al. 2021), the major factors controlling sea ice advance in the Chukchi Sea in early winter and its predictability have yet to be fully assessed. Summertime Arctic SIA has decreased drastically over the past several decades (Cavalieri and Parkinson 2012); therefore, the recent delay in freezing-up in the Chukchi Sea in early winter might be related to the initial condition of reduced summertime sea ice cover and/or other factors. In this study, we examined the seasonal predictability of sea ice in the Chukchi Sea in early winter using model simulations, and we explored the possible mechanisms responsible for the skillful prediction over the past several decades (1979–2016), including the abnormally low SIA in 2016, with special emphasis on year-to-year variability. To achieve our objective, canonical correlation analysis was used as a forecasting and diagnostic tool to explore the physical mechanism between the predictors (atmosphere–ocean variables) and the predictand (sea ice concentration).

## 2. Data and methods

### a. PIOMAS

In this study, we used the Pan-Arctic Ice–Ocean Modeling and Assimilation System (PIOMAS) dataset from 1979 to 2016 (Zhang and Rothrock 2003) for the canonical correlation analysis (CCA) predictand (sea ice) and predictors. PIOMAS is an ice–ocean coupled model based on the POP ocean model (Smith et al. 1992) and a 12-category thickness and enthalpy distribution sea ice model (Zhang and Rothrock 2001) in a generalized orthogonal curvilinear coordinate system for the Arctic Ocean. The spatial coverage is  $\sim 49^{\circ}$ – $90^{\circ}$ N and lateral boundary conditions are input from a global model governed by the same configuration as PIOMAS (Zhang and Rothrock 2003). The mean horizontal resolution of PIOMAS for the Arctic Ocean is approximately 22 km with 30 vertical ocean levels of different thickness. The model is driven by daily mean NCEP–NCAR atmospheric reanalysis data (Kalnay et al. 1996), which comprise 10-m surface winds, 2-m surface air temperature, specific humidity, precipitation, evaporation, downward longwave radiation, sea level pressure (SLP), and cloud cover. Surface heat and momentum fluxes are calculated using the bulk formula with these meteorological variables. Downward shortwave radiation is calculated from the cloud cover in accordance with Parkinson and Washington (1979). After performing a 30-yr spinup of the model based on atmospheric reanalysis data for 1948, the model was driven from 1948 to 1978 without data assimilation to generate the initial conditions of PIOMAS. From 1979, the PIOMAS hindcast was driven using the daily mean NCEP–NCAR atmospheric reanalysis data and assimilation of daily mean sea ice concentration (SIC) from the NSIDC near-real time products (Brodzik and Stewart 2016) and daily

mean SST (Reynolds et al. 2007; also see Schweiger et al. 2011).

As for the CCA predictand, we adopted the 2-month averaged SIC in the Chukchi Sea (65°–75°N, 180°–160°W) in early winter (November–December) to examine the predictability of sea ice advance in early winter. Any grid cell at which SIC was zero during the entire analysis period was not used. We used 2-month averaged ice–ocean heat variables as the predictors of the SIC. The SIC predictors adopted comprised sea ice production ( $Q_{ice}$ ), sea ice advection ( $ADV_{ice} = -\mathbf{v}_i \cdot \nabla h_i$ ) that was calculated from sea ice velocity ( $\mathbf{v}_i$ ) and sea ice thickness ( $h_i$ ), and total surface heat flux at the ocean–atmosphere or sea–ice interface ( $Q_{sfc}$ ), which consists of turbulent and radiative heat fluxes. Additional predictors included ocean heat content ( $HC = \int_{sfc}^{55} \rho_o C_p T dz$ ) and lateral ocean heat advection ( $ADV = -\int_{sfc}^{55} \mathbf{v} \cdot \nabla T dz$ ), where  $\mathbf{v}$  and  $T$  are ocean velocity and temperature, respectively, integrated from the surface to 55-m depth, which broadly corresponds to the mean depth of the Chukchi Sea. Examination of these thermodynamic terms allowed identification of the physical processes responsible for SIC variability. We also evaluated the persistency of the sea ice itself by using SIC anomalies in each month. Although the energy budget for sea ice production and latent heat for melting at the sea–ice interface is not perfectly consistent owing to the data assimilation procedure, the homogeneity of the ice–ocean model output and its reliability, as shown in the following section, is suitable for empirical prediction using CCA. The original model grid was bilinearly interpolated to a  $0.5^\circ \times 0.5^\circ$  grid size before CCA was conducted.

### b. CCA

Canonical correlation analysis is a multivariate statistical technique used to identify linear correlation relationships between multidimensional variables. In the climate research community, CCA is commonly used both for extraction of the dominant coupled patterns between the predictor and the predictand from atmospheric and oceanic data (Bretherton et al. 1992) and for seasonal climate forecasting (Zwiers and von Storch 2004) and research on sea ice predictability (Tivy et al. 2011; Nakanowatari et al. 2014, 2015). In this study, we followed the methodology and data processing adopted by Barnett and Preisendorfer (1987), whereby predictor and predictand data were standardized by subtracting the mean value of the analyzed period and dividing anomalous values with the standard deviations. Then, a prefiltering procedure was applied to the predictor and predictand data using principal component analysis (PCA), following which the linear trend components were removed. Noise was removed from the obtained series of PCs using Monte Carlo techniques to obtain the significant principal modes, and it was these derived PC modes that were used for CCA. The Monte Carlo techniques were conducted using 100 surrogate data with temporal variation of white noise, and then the significant PCs for the predictand and the predictor were determined by the

value of the explained variance larger than the top 95% of that for the surrogate data. The mathematical representation of CCA is described in appendix. Because SIC in November–December is affected by the integration of the preceding atmospheric and oceanic forcings, we adopted 2-month averages for the predictors in accordance with earlier related studies (Nakanowatari et al. 2014, 2015). CCA was conducted between SIC in November–December and the 2-month average predictors at lead times from 0 (November–December) to 11 months (previous December–January) to evaluate the predictability at given lead times.

The forecast skill for each predictor was evaluated using field-averaged cross-validated correlation between the observed and modeled data. Field-averaged cross-validated correlation is a standard metric used to evaluate the skill of CCA-based forecasting models (e.g., Barnston 1994). In this procedure, each of the 37 years from 1980 to 2016 was held out in turn, while the remaining 36 years were used for CCA. The entire sequence of the CCA procedure was performed for each case to obtain the predicted SIC in the entire analyzed period. The field-averaged cross-validated correlation was calculated by averaging the correlation between the observed and predicted SIC at each grid point over the analyzed area. This cross-validation scheme is commonly used to prevent overfitting of statistical prediction models (Michaelsen 1987; Elsner and Schmertmann 1994).

The significance of local skill (skill at a single grid point) was determined using a Monte Carlo simulation, which involved a phase randomization technique that generated 1000 surrogate time series (Kaplan and Glass 1995). First, absolute Fourier amplitudes (square root of spectra) for the observed SICs were estimated for each grid point, and then the 1000 surrogate time series were generated via an inverse Fourier transform with the observed Fourier amplitudes and randomized phases. Surrogate correlation coefficients were estimated between the surrogate and observed SIC time series. The relative position of the absolute value of the observed correlation coefficients in the sorted absolute values of the surrogate correlation coefficients provided the level of confidence regarding the observed correlation coefficient at each grid point.

### c. Observational data

For evaluation of the interannual variability of sea ice in the Chukchi Sea using PIOMAS, we used satellite-based SIC derived from *Nimbus-7* SMMR and DMSP SSM/I-SSMIS passive microwave data with the revised NASA team algorithm for 1979–2016 (Cavalieri et al. 1996). This satellite-based SIC dataset is identical to the SIC dataset assimilated in PIOMAS in terms of the sea ice algorithm and satellite sensor type, except that the former comprises processed and quality-controlled data of long-term dataset. The spatial resolution is 25 km on a polar-stereographic coordinate system. Before undertaking comparison of the satellite-based SIC and the PIOMAS hindcast SIC data, the daily mean satellite-based SIC data were averaged over each month and bilinearly interpolated to a  $0.25^\circ \times 0.25^\circ$  grid. For validation of the ocean

temperature and current field in the PIOMAS data, we used time series mooring observations of ocean temperature and current speed recorded near the bottom at station A3 in the Bering Strait obtained during 1990–2016 (Woodgate et al. 2015; Woodgate 2018; Woodgate and Peralta-Ferriz 2021). Station A3 is located in the north of the strait, which is an area influenced by the water properties of both eastern and western channels; thus, it is known to be representative of the entire throughflow (Woodgate et al. 2005, 2006).

To explore the source of sea ice predictability and its relation to the atmospheric circulation pattern, we used monthly mean NCEP–NCAR reanalysis data from 1979–2016, which are identical to the atmospheric forcing of the PIOMAS hindcast. The meteorological variables used in this study were surface wind stress, 2-m air temperature, 10-m wind speed, SLP, and 500-hPa geopotential height. Generally, the drag coefficient of surface wind stress is influenced by the existence of sea ice (Leppäranta 2005). Therefore, in comparison with the other meteorological variables, there would appear to be uncertainty in the wind stress data attributable to the atmospheric boundary layer conditions in the sea ice area. Moreover, the atmospheric reanalysis surface wind data in winter have large uncertainty owing to the limited observational data in comparison with the data availability in summer (Inoue et al. 2009; Nose et al. 2018). To assess our results, we also used ERA-Interim monthly mean wind stress data on a  $0.75^\circ \times 0.75^\circ$  grid from 1979 to 2016 (Dee et al. 2011).

### 3. Chukchi Sea ice variability in early winter (1979–2016)

First, we present the spatial distribution of the sea ice edge in the Chukchi Sea for 1979–2016 in early winter derived from satellite-based observations (Fig. 1). In this season, the location of the sea ice edge largely fluctuates from the Bering Sea ( $\sim 63^\circ\text{N}$ ) to the northern Chukchi Sea ( $\sim 72^\circ\text{N}$ ). However, the fraction of the open-water area in the Chukchi Sea has increased since the 2000s, consistent with the trend of surface air temperature over the Chukchi Sea in winter (Kug et al. 2015). The time series of averaged SIA in the Chukchi Sea shows that the interannual variability of SIA in early winter has decreased similarly to that in summer (Fig. 1b). In particular, the year-to-year fluctuations of SIA in early winter coincided with those in summer in the 1980s to mid-1990s. The correlation between SIA in early winter and summer is 0.57 ( $P = 0.008$ ) for 1979–97. If the linear trend component is removed from these time series, the correlation between them is reduced to 0.49 ( $P = 0.034$ ) but it remains significant at the 95% confidence level. This result indicates that sea ice advance in early winter can be explained by the initial condition of the summertime SIA for this period, although recent numerical modeling studies showed that the summertime SIA itself is not skillfully predicted before spring (Bonan et al. 2019; Bushuk et al. 2020). However, summertime SIA has been relatively low since the late 1990s, and the above correlation relationship is weakened. The 2-month lagged autocorrelation of SIA anomalies is not statistically significant ( $r = 0.37$ ,  $P = 0.159$ ) from 1998 onward. These results suggest that interannual variability of SIA in the Chukchi Sea in early winter is not well

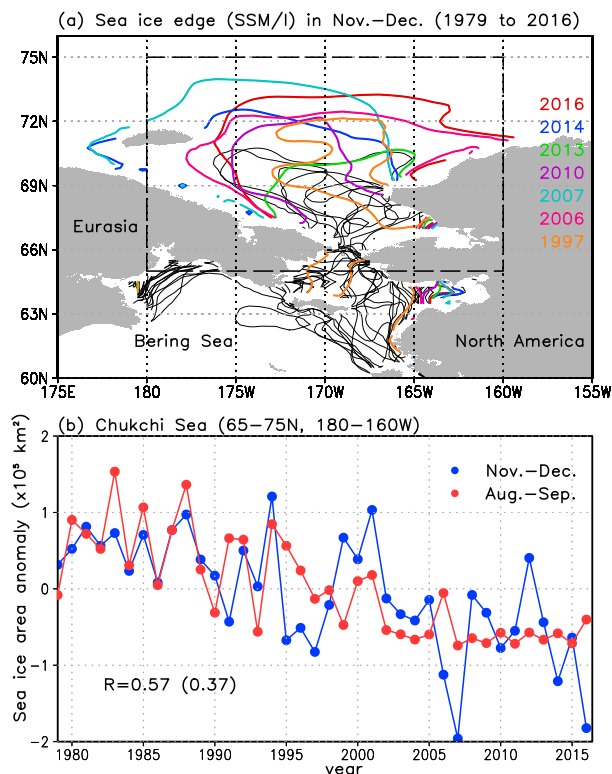


FIG. 1. (a) Sea ice edge distribution (contours) of satellite-based observations in early winter (November–December) from 1979 to 2016. The sea ice edge is defined as the boundary of the 40% SIC averaged in early winter. Sea ice edges in those years with low sea ice extent (i.e., 1997, 2006, 2007, 2010, 2013, 2014, and 2016) in the Chukchi Sea are shown by colors. (b) Time series of SIA anomalies in the Chukchi Sea ( $65^\circ$ – $70^\circ\text{N}$ ,  $180^\circ$ – $160^\circ\text{W}$ ) in November–December (red) and August–September (blue) from 1979 to 2016. The SIA anomalies are defined by the SIA relative to the climatological mean values from 1979 to 2016. The correlation coefficient between the time series is shown in (b) and the value in parentheses is for the detrended time series.

explained by the persistence of the sea ice condition in the preceding summer in recent decades.

### 4. Sea ice and ocean temperature states in PIOMAS

Here, we show the mean state and interannual fluctuations of the ice–ocean variables of PIOMAS with special emphasis on the Chukchi Sea. The climatological SIC distribution and the standard deviation of SIC anomalies in early winter (November–December) during 1979–2016 for the satellite-based observations and PIOMAS are shown in Figs. 2a and 2b, respectively. It is confirmed that the climatological sea ice distribution of PIOMAS is very similar to that of the satellite-based observations with SIC of 50%–90% within the Chukchi Sea (Fig. 2a). The prominent interannual variability of the satellite-based SIC in the northern Chukchi Sea ( $72^\circ\text{N}$ ,  $170^\circ\text{W}$ ) is well reproduced in PIOMAS (Fig. 2b). The PIOMAS SIC also quantitatively tracks the temporal variability in SIA in



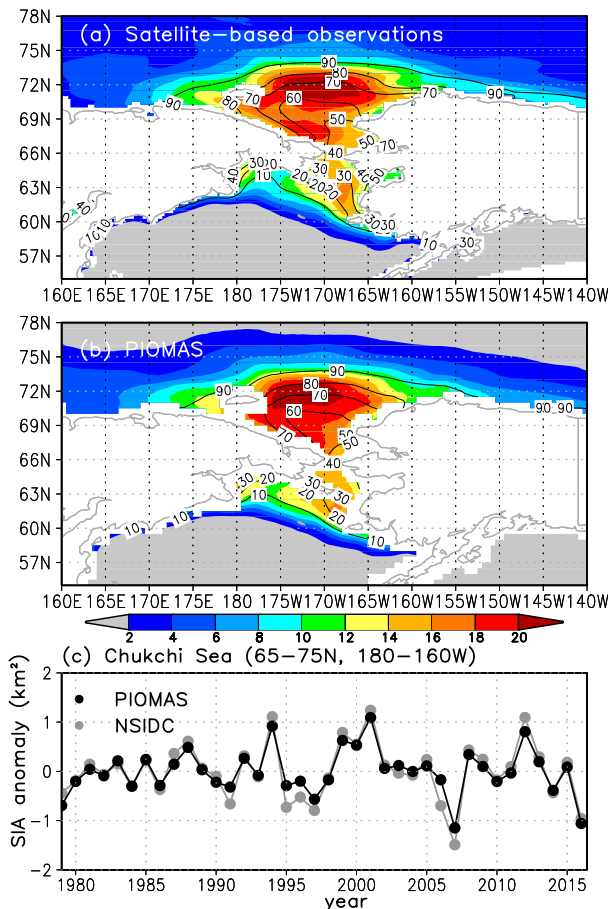


FIG. 2. Climatological monthly mean SIC (%; contours) and standard deviation of the interannual variability (colors) in early winter (November–December) from (a) satellite-based observations and (b) PIOMAS from 1979 to 2016. (c) Time series of SIA anomalies in the Chukchi Sea (65°–70°N, 180°–160°W) for satellite-based observations (gray) and PIOMAS (black) in early winter (November–December) from 1979 to 2016.

the Chukchi Sea (65°–70°N, 180°–160°W) when compared with the satellite-based observations ( $r = 0.96$ ,  $P < 0.001$ ; Fig. 2c). The reliability of the spatiotemporal variability of PIOMAS SIC confirms that such hindcast data are appropriate for examination of the interannual variability of SIC in the Chukchi Sea.

To evaluate the climatological distribution of PIOMAS upper-ocean temperature in and around the Chukchi and Bering Seas, the climatological distribution of the annual mean subsurface ocean temperature at 22-m depth is shown in Fig. 3a, in which the observed data are not assimilated. The relatively warm water moving from the Bering Sea to the Chukchi Sea along the west coast of Alaska indicates that advective heat fluxes associated with the Bering Strait volume transport are well reproduced in PIOMAS, despite the reasonably coarse grid size. Time series of ocean temperature anomalies near the bottom of the Bering Strait in the mooring data and PIOMAS in summer (August–September) are

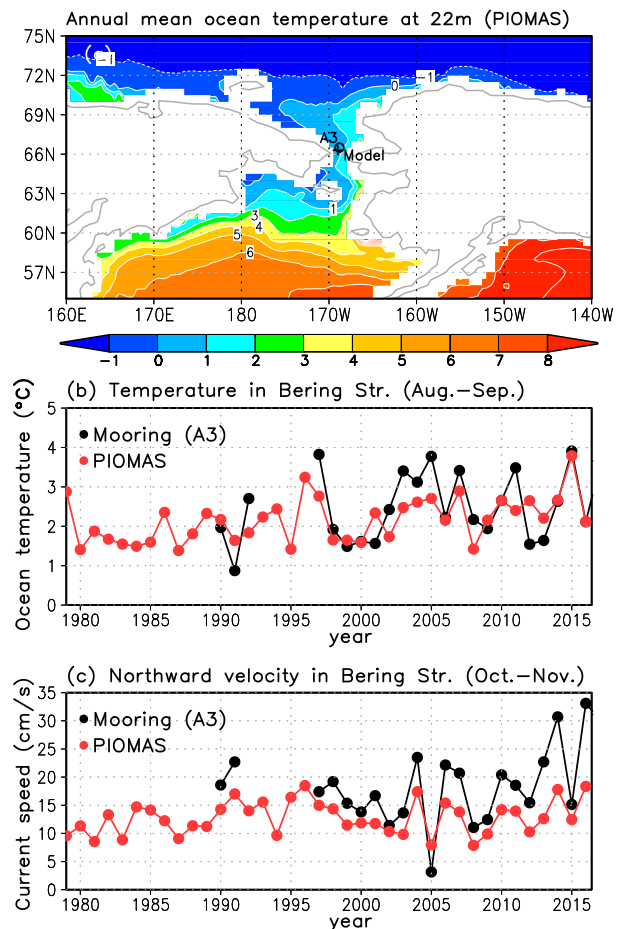


FIG. 3. (a) Climatological annual mean of subsurface ocean temperature at 22 m derived from PIOMAS for 1979–2016. The cross mark indicates the location of mooring station A3 north of the Bering Strait (Woodgate et al. 2006). (b) Time series of potential temperature near the bottom for A3 mooring observations (black) for 1990–2016 and potential temperature at 27–55-m depth (bottom depth) of PIOMAS (red) for 1979–2016 in August–September. (c) Time series of northward current speed near the bottom for A3 mooring observations (black) for 1990–2016 and northward current speed averaged from the surface to the bottom depth of PIOMAS (red) for 1979–2016 in October–November.

illustrated in Fig. 3b. In summer, ocean heat transport via the Bering Sea Throughflow is known to be a precondition of the ocean heat content (HC) in the Chukchi Sea in early winter (Serreze et al. 2016). The interannual variability of the ocean temperature is quantitatively reproduced in PIOMAS; the correlation between the observed and PIOMAS ocean temperature anomalies is 0.75. PIOMAS also realistically reproduces the interannual variability of the ocean current speed in the Bering Strait in autumn (October–November). The vertically averaged northward current speed in the Bering Strait in PIOMAS is correlated significantly with the observed current speed near the bottom ( $r = 0.91$ ), although the absolute velocity in PIOMAS is somewhat underestimated (Fig. 3c). This might be related to the fact that the spatial resolution of

PIOMAS is insufficient to represent the narrow current structure of the Bering Strait volume transport. However, the PIOMAS-simulated mean volume transport in the Bering Strait ( $0.80 \text{ Sv}$ ;  $1 \text{ Sv} \equiv 10^6 \text{ m}^3 \text{ s}^{-1}$ ) is close to the observed estimation ( $0.81 \text{ Sv}$ ) (Grebmeier and Maslowski 2014). These comparisons confirm that the interannual signals of ocean temperature and current field, and the related volume and heat transport, in the Chukchi Sea are reasonably represented in PIOMAS and thus that this long-term historical dataset is suitable for the purpose of our study.

### 5. Prediction skill for Chukchi Sea ice in early winter

Prediction skill for each predictor at the corresponding forecast lead times, evaluated by the area-averaged value of the cross-validated correlation between the predicted and simulated SICs in the Chukchi Sea in early winter, is shown in Fig. 4. The highest prediction skill is obtained from SIC persistence at the lead time of 1 month, but the prediction skill decreases at lead times of 2–3 months, consistent with the insignificant correlation between SIA in the Chukchi Sea in summer and early winter from 1998 (Fig. 1b). Except for the persistence of SIC itself, relatively high prediction skill is obtained from  $Q_{ice}$  and ocean HC predictors at the 1-month lead time, indicating that local sea ice production, which is related to the oceanic thermal condition, determines SIC (i.e., sea ice advance) rather than the advection of sea ice ( $ADV_{ice}$ ). At the 2-month lead time (September–October), the maximum forecast skill is obtained from ocean HC, and it is comparable with that from SIC; the forecast skill for both the  $Q_{sfc}$  and ADV predictors is significant and higher than that for both  $Q_{ice}$  and  $ADV_{ice}$ . This result indicates that  $Q_{sfc}$  and ADV are responsible for the significant prediction skill for HC at the 2-month lead time and  $Q_{ice}$  at the 1-month lead time. It is noteworthy that meaningful prediction skill is also found at 4- and 5-month lead times (June–July and July–August) for ADV and  $Q_{sfc}$ , although these signals are related to the transient signal attributable to the minimum SIA recorded in summer 2007 (Stroeve et al. 2008). Except for the high prediction skill at 4- and 5-month lead times attributable to the minimum sea ice event in 2007, the 2-month leading  $Q_{sfc}$  and ADV including HC, is essential for predicting sea ice production and useful for seasonal prediction of sea ice advance in the Chukchi Sea for the past 37 years.

The spatial distribution of CCA skill for SIC in early winter as predicted by the 2-month leading major predictors and 1-month leading  $Q_{ice}$  is shown in Fig. 5. For the 2-month leading HC predictor, the significant prediction skill with a cross-validated correlation of  $>0.4$  is found in the northern part of the Chukchi Sea, covering 66% of the analyzed area. This spatial distribution of significant prediction skill resembles that for the 2-month leading ADV predictor (Fig. 5c), although the significant prediction skill is found mainly in the northwestern Chukchi Sea, which covers 55% of the analyzed area. The CCA skill distribution for the 2-month leading ADV and HC is largely overlapped, indicating that the ocean heat conditions responsible for SIC predictability are closely related to lateral advection of ocean heat flux (i.e., ADV).

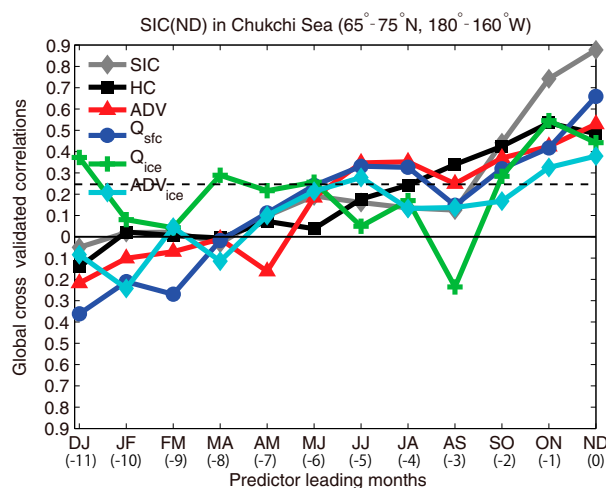


FIG. 4. Forecast skill (global cross-validated correlation) of SIC (November–December) in the Chukchi Sea ( $65^{\circ}$ – $75^{\circ}$ N,  $180^{\circ}$ – $160^{\circ}$ W) for 0-month (November–December) to 11-month (December–January) lead times from SIC (gray), ocean HC (black), ADV (red),  $Q_{sfc}$  (blue),  $Q_{ice}$  (green), and  $ADV_{ice}$  (cyan). Horizontal solid and dashed lines indicate the zero value and the 95% confidence level, respectively.

The CCA skill for SIC predicted by the 2-month leading  $Q_{sfc}$  predictor (Fig. 5b) shows that significant forecast skill is found over the southern or southeastern Chukchi Sea, covering 43% of the analyzed area. For the 1-month leading  $Q_{ice}$  predictor (Fig. 5d), significant prediction skill covers the entire region of the Chukchi Sea. These results indicate that the 2-month leading ocean heat advection and surface heat flux independently influence SIC in early winter (i.e., sea ice advance) in the Chukchi Sea through change in the 1-month leading sea ice production. In the following section, the source of SIC predictability related to the 2-month leading  $Q_{sfc}$  and ADV is examined diagnostically from the temporal and spatial patterns of the leading CCA modes.

### 6. Source of predictability

Evaluation of the forecast skill clarified that the two predictors of the 2-month leading  $Q_{sfc}$  and ADV (September–October) are the determinant factors for predicting sea ice advance in early winter. The statistics for the CCA calculations (i.e., the PC modes, CCA truncation points, and squared canonical correlations) are summarized in Table 1. The CCA truncation points reflect the number of EOF modes for the predictors and predictands, which are in turn adopted for the CCA calculation. The canonical correlation is the correlation between the predictor and the predictand time series for each CCA mode, and its squared values indicate the contribution of each CCA mode to the total variance of the predictand. In both predictor cases (2-month leading  $Q_{sfc}$  and ADV), the squared canonical correlations for first CCA mode (CCA1) are distinctly large (0.69 and 0.63, respectively). Therefore, we examine the spatiotemporal patterns for

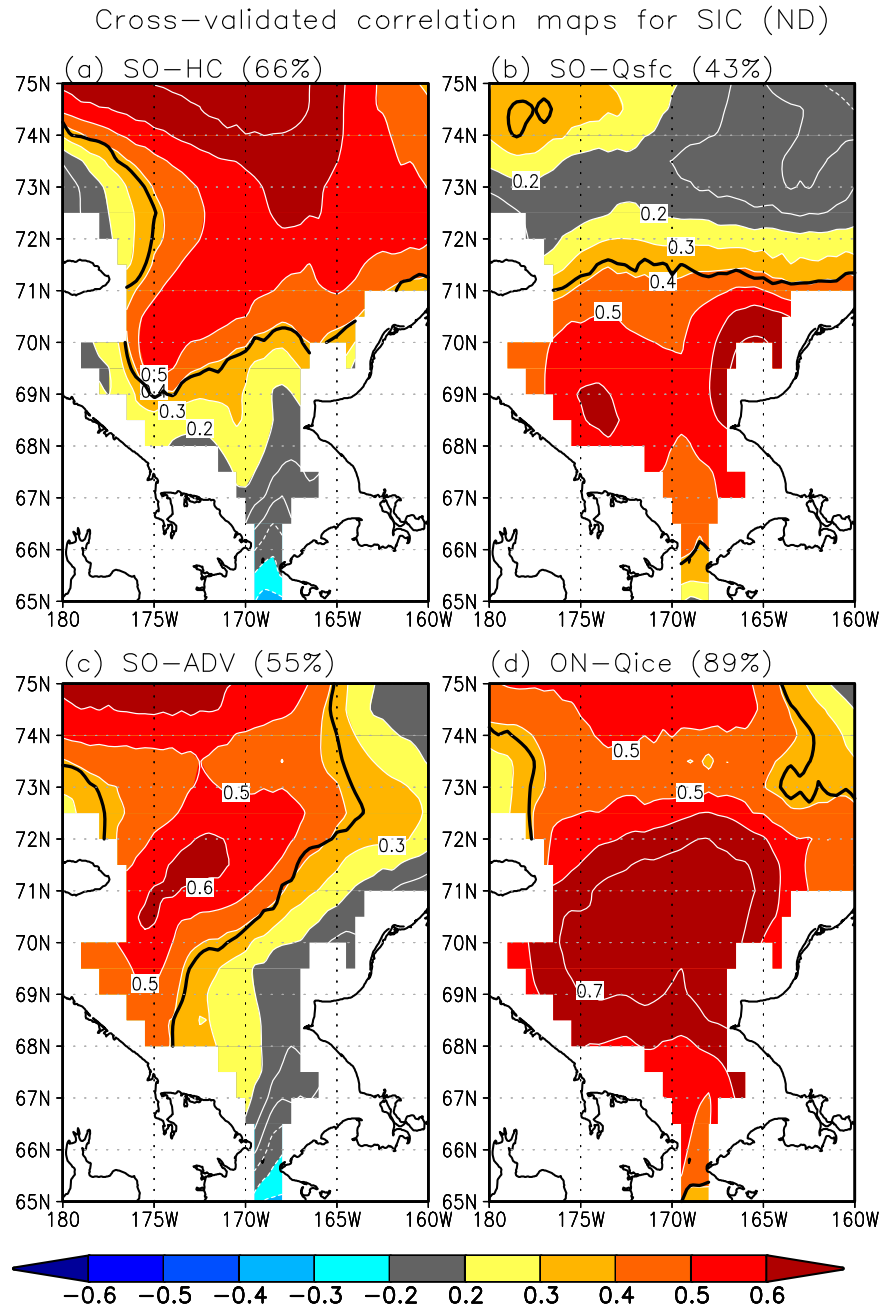


FIG. 5. Spatial distribution of CCA skill (cross-validated correlation between the SIC and predicted SIC) for 2-month leading forecast from (a) ocean HC, (b)  $Q_{sfc}$ , and (c) ADV, and for 1-month leading forecast from (d)  $Q_{ice}$ . Bold contour (black) indicates the area where the cross-validated correlation is significant at the 95% confidence level.

CCA1 to identify the source of SIC predictability in the following subsections.

*a.  $Q_{sfc}$  predictor case (September–October)*

The canonical correlation maps and time series for the leading CCA mode (CCA1), shown in Fig. 6, are the spatial distribution of the correlation coefficients between the canonical

correlation time series of  $Q_{sfc}$  for CCA1 and the reconstructed SIC of four EOF modes. Because 40% of the total SIC variance is explained by CCA1 (Table 1), CCA1 is the source of predictability in  $Q_{sfc}$  related to SIC prediction skill. The canonical correlation pattern of  $Q_{sfc}$  in CCA1 shows significant negative values higher than  $-0.8$ , in the southeastern Chukchi Sea (Fig. 6a), where the canonical correlation of SIC

TABLE 1. PC and CCA truncation points for each predictor case. The percentage of the original variance in the predictand and the predictor retained after PC truncation and the percentage of the original variance in the predictand explained by each CCA mode are shown in parentheses.

	Truncation points (percent variance explained)			Canonical correlation <sup>2</sup> (percent predictand variance explained)			
	PC-ND SIC	PC-predictor	CCA	CCA1	CCA2	CCA3	CCA4
$Q_{\text{sfc}}$	4 (89)	6 (69)	4	0.69 (40)	0.46 (27)	0.27 (15)	0.12 (7)
ADV	4 (89)	8 (67)	4	0.63 (39)	0.54 (33)	0.23 (14)	0.04 (3)

shows positive values (Fig. 6b). The climatological upward surface heat flux in September–October is prominent at more than  $100 \text{ W m}^{-2}$  in the southeastern Chukchi Sea (Fig. 7a); therefore the negative correlation between SIC and  $Q_{\text{sfc}}$  in the canonical correlation map indicates that autumn preconditioning of the atmospheric cooling anomaly leads to sea ice advance in the eastern Chukchi Sea. The canonical correlation time series of CCA1 exhibits remarkable year-to-year variability (Fig. 6c), and the positive SIC anomalies in 1994, 1999, and 2001 are related to the distinct increase in surface cooling in September–October. The averaged SIA in the Chukchi Sea in early winter shows distinct positive anomalies in 1994, 1999, and 2001, but the preceding summertime SIA anomaly is relatively low except for 1994. This result suggests that the SIAs in early winter in the years of 1999 and 2001 are caused by the anomalous heat loss in autumn rather than the persistence of summertime sea ice condition.

Climatological atmospheric conditions indicate that the northeasterly wind is prominent over the Chukchi Sea where surface air temperature is  $<0^\circ\text{C}$  in September–October (Fig. 7b); therefore, the northeasterly cold wind anomaly is considered a possible cause of the upward surface heat flux (cooling). To understand the mechanism of the atmospheric cooling process in relation to the leading CCA mode for  $Q_{\text{sfc}}$ , we conducted regression analysis of the meteorological variables (surface wind speed and air temperature) related to turbulent heat flux onto the predictor canonical correlation time series. The regression map of surface wind and air temperature in the NCEP–NCAR reanalysis against the canonical correlation time series of CCA1 is shown in Fig. 8a. The leading CCA mode for  $Q_{\text{sfc}}$  in the Chukchi Sea is related to both the northeasterly wind anomaly and the negative surface air temperature anomaly associated with the cyclonic circulation pattern over the Gulf of Alaska.

Because the northeasterly wind anomaly is related to the cyclonic circulation anomaly over the Gulf of Alaska (Fig. 8a), which is likely related to the atmospheric teleconnection pattern such as the Pacific–North American pattern (Barnston and Livezey 1987), we investigated the atmospheric circulation pattern related to the northeasterly wind anomaly in terms of the atmospheric teleconnection pattern. The regression map of 500-hPa geopotential height (z500) against the canonical component time series of CCA1 for  $Q_{\text{sfc}}$  is shown in Fig. 9. The northeasterly wind anomaly over the Chukchi Sea is related to the negative anomaly over the Gulf of Alaska, which is accompanied by positive anomalies over the subarctic North Pacific and North America. To check the relationship between the dominant teleconnection patterns in the North

Pacific and the leading CCA mode for  $Q_{\text{sfc}}$ , we calculated the correlations between the canonical correlation time series of CCA1 and the major teleconnection pattern indexes in the Northern Hemisphere (NOAA CPC 2021). We obtained significant correlation between the canonical component time series of CCA1 and the east Pacific–North Pacific index in October ( $r = 0.47$ ) at the 95% confidence level. Thus, when the east Pacific–North Pacific pattern is in the negative phase, the northeasterly wind over the Chukchi Sea leads to ocean preconditioning preferential for sea ice advance in early winter.

#### b. ADV predictor case (September–October)

The canonical correlation maps and time series for CCA mode 1 (CCA1) of ADV in September–October, which explain 39% of the original variance of SIC (Table 1), are shown in Fig. 10. Significant positive correlation for ADV is zonally found around  $71^\circ\text{--}72^\circ\text{N}$  (Fig. 10a), where significant negative correlation for SIC is found (Fig. 10b). This result indicates that the ocean heat flux convergence set up in September–October suppresses sea ice advance in the Chukchi Sea in early winter. The canonical correlation time series exhibits a remarkable negative anomaly of SIC in 1991, 1995, and 2016, which is related to excess ocean heat advection, indicating that the abnormal delays in sea ice advance in these years were related to lateral ocean heat advection in autumn (Fig. 1b). It is noteworthy that the canonical correlation time series for ADV shows a remarkable negative anomaly in 2012 when the summertime sea ice extent in the Arctic Ocean reached a record minimum (Parkinson and Comiso 2013). This result implies that suppressed ocean heat flux convergence in late autumn was related to the substantial sea ice advance in early winter despite a low sea ice condition in summer.

The physical mechanism controlling ADV in the northern Chukchi Sea is considered to involve local change in ocean currents and advection of the upstream temperature anomaly. Here, we evaluate the influence of change of the local currents on the ADV signal in the northern Chukchi Sea using ocean velocity and sea surface height (SSH) in September–October. The regression map of surface ocean currents in September–October onto the canonical correlation time series of ADV is shown in Fig. 11a. The northward current anomaly is prominent in the entire Chukchi Sea with a maximum in the Bering Strait, indicating that increase in the volume transport in the Bering Strait is related to ocean heat flux convergence within the Chukchi Sea. The regression map of SSH in September–October shows a significant negative anomaly that extends along the coastal area of the East



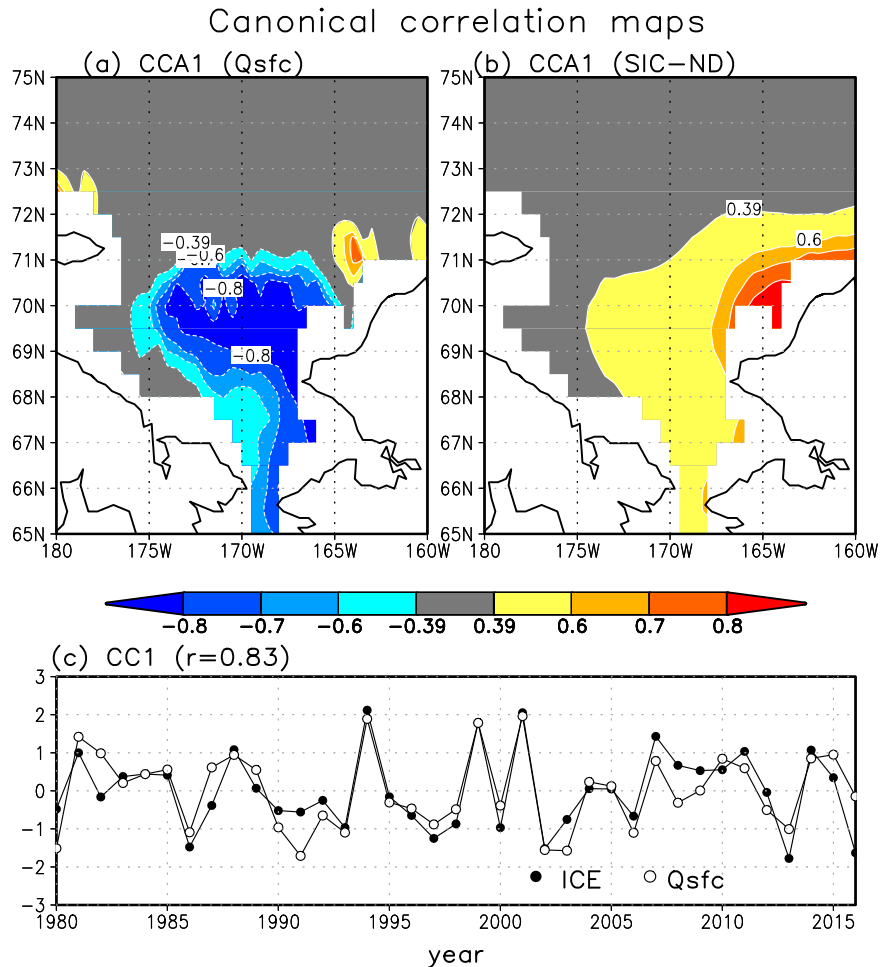


FIG. 6. CCA mode 1 of 2-month leading  $Q_{sfc}$  predictor case. Canonical correlation map of (a)  $Q_{sfc}$  (September–October) and (b) SIC (November–December), and (c) the time series of the canonical correlation for  $Q_{sfc}$  and SIC. The canonical correlation between them is 0.83. Colored regions in (a) and (b) indicate areas where the correlations are significant at the 95% confidence level.

Siberian Sea (ESS) (Fig. 11b). This result indicates that the Bering Strait volume transport in September–October is predominantly controlled by barotropic adjustment of sea level change in the Arctic Ocean, particularly in the ESS. The significant sea level change in the ESS and the relation to Bering Strait volume transport is consistent with an earlier study based on satellite-based bottom pressure data from the Gravity Recovery and Climate Experiment (GRACE; Peralta-Ferriz and Woodgate 2017). We examined the impact of the ocean temperature anomaly on the ADV signal in the northern Chukchi Sea through lead-lag correlation analysis between SST and the canonical correlation time series of ADV; however, the influence of anomalous ocean temperatures was weak in this area (not shown).

The dominant controlling factors of volume transport in the Bering Strait are considered to comprise the dynamical balance of the pressure head difference between the North Pacific and the Arctic Ocean and the locally induced wind-

driven ocean current system (Woodgate et al. 2012). Negative SSH anomaly is found over the continental shelf with an amplified signal from the ESS to the Bering Strait (Fig. 11b). The pattern of amplification of the SSH anomaly along the coast is similar to the characteristics of the dynamical response of SSH caused by arrested topographic waves (ATWs) (Csanady 1978), which are prominent in the subarctic North Pacific in winter (Qiu 2002, Nakanowatari and Ohshima 2014). Here, we examine the application of ATW theory to the interannual variability of volume transport in the Bering Strait in September–October and compare it with that derived from the PIOMAS ocean current speed.

According to Csanady (1978), the alongshore volume transport of ATWs ( $V_{ATW}$ ), which occurs in a steady manner, can be determined as follows:

$$V_{ATW} = \int_{l_1}^{l_2} \frac{\tau_L}{\rho f} dl, \quad (1)$$

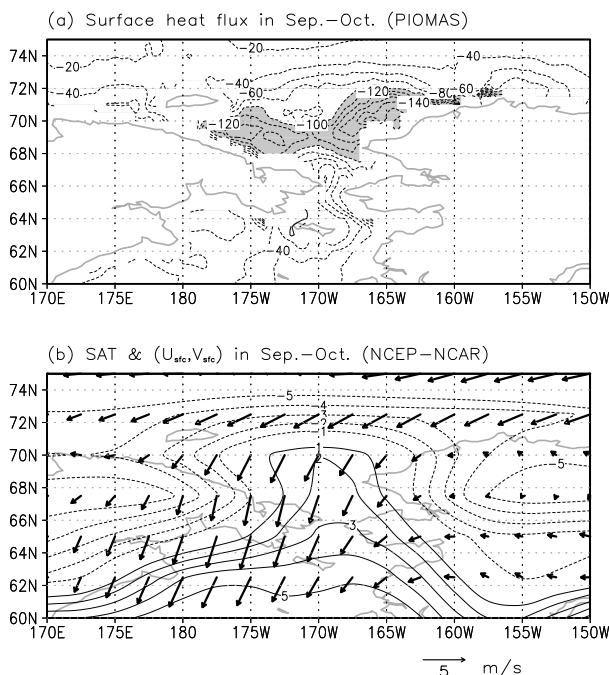


FIG. 7. Climatological (a) total surface heat flux ( $\text{W m}^{-2}$ ) and (b) 2-m surface air temperature ( $^{\circ}\text{C}$ ; contours) and 20-m surface wind ( $\text{m s}^{-1}$ ; vectors) in September–October derived from NCEP–NCAR reanalysis for 1979–2016. In (a), negative values mean upward, and the region where the absolute value is  $>100 \text{ W m}^{-2}$  is shaded.

where a right-handed coordinate system is used with the  $l$  axis along the coastline,  $\tau_l$  is the alongshore component of wind stress,  $\rho$  is the density of water, and  $f$  is the Coriolis parameter. On time scales longer than 1 month, the volume transport of the coastally trapped flow is determined by Eq. (1), which can be derived from the linear momentum equation (or vorticity equation) in a stationary state. It is this steady flow that Csanady (1978) called an ATW. This equation implies that the alongshore transport at  $l_1$  is the sum of the Ekman transport to or from the coast over the integral route from the starting point of  $l_2$  to  $l_1$ . The integral route of the Ekman transport depends on several factors, such as the shape of the coastline, shelf width, shelf slope, and bottom friction, which are difficult to identify (Csanady 1978). Considering that the significant negative SSH anomaly signal is extended to  $\sim 175^{\circ}\text{E}$ , we calculated the ATW transport in the Bering Strait (labeled BS in Fig. 11b) along the coast of the ESS from  $175^{\circ}\text{E}$  [labeled S (for starting point) in Fig. 11b].

The correlation between the time series of the volume transport in the Bering Strait in PIOMAS and the ATW calculated from the wind stress data of the NCEP–NCAR reanalysis is found to be 0.69 from 1980 to 2016 (significant at the 95% confidence level). The amplitude of the detrended ATW transport anomalies in September–October is comparable with that of the detrended volume transport anomalies in the Bering Strait on a year-to-year time scale (Fig. 12a). This result demonstrates that the interannual variability of the volume transport in the Bering Strait is explained quantitatively

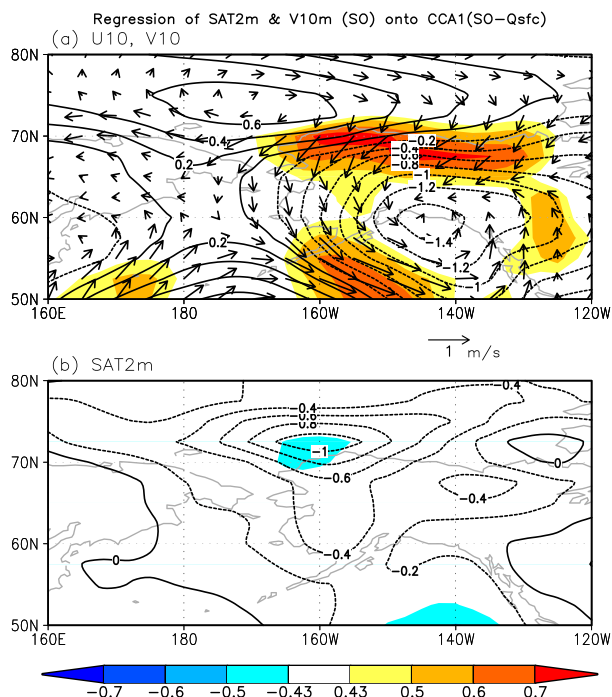


FIG. 8. Regression of (a) September–October 10-m surface wind speeds ( $\text{m s}^{-1}$ ; vectors) and SLP (hPa; contours) and (b) 2-m surface air temperature ( $^{\circ}\text{C}$ ; contours) onto  $Q_{\text{sfc}}$  canonical correlation time series for CCA1. The correlations of wind speed and surface air temperature where the canonical correlation time series exceeds the 95% confidence level are also shown by color shading.

by ATW theory. We also examined ATWs on the basis of ERA-Interim wind stress data, and the obtained results are almost identical to those derived using NCEP–NCAR reanalysis data (Table 2). The ATW transport in September–October is also significantly correlated with the detrended SIA in the Chukchi Sea in early winter ( $r = -0.55$ ; Fig. 12a and Table 2); therefore, this quantity may be used for seasonal prediction of the volume transport in autumn and the sea ice advance in early winter.

It is noteworthy that the interannual variability of SIA in the Chukchi Sea in November–December is highly correlated with ATW variability in September–October after 2000 (Table 2). For example, the Arctic SIA in summer 2012 was a record minimum of past decades and the ice retreat was particularly pronounced in the Pacific sector, including the Chukchi Sea (Parkinson and Comiso 2013); however, the SIA anomaly in the Chukchi Sea in early winter was relatively large in 2012 (Figs. 1a and 12a). This positive SIA anomaly was consistent with the remarkable low value of the Bering Strait volume transport and ATW anomaly ( $-0.20 \text{ Sv}$ ), which led to suppressed advection of ocean heat flux in autumn (September–October) and promoted sea ice advance in early winter. Conversely, in 2016, the ATW anomaly in September–October was  $0.3 \text{ Sv}$  (i.e., the largest value of the past 38 years) and the SIA anomaly in the Chukchi Sea was the second lowest value, even when the linear trend was removed (Fig. 12a). When linear trends are included in the ATW and volume

Z500 (SO) onto CCA1 (Qsfc)

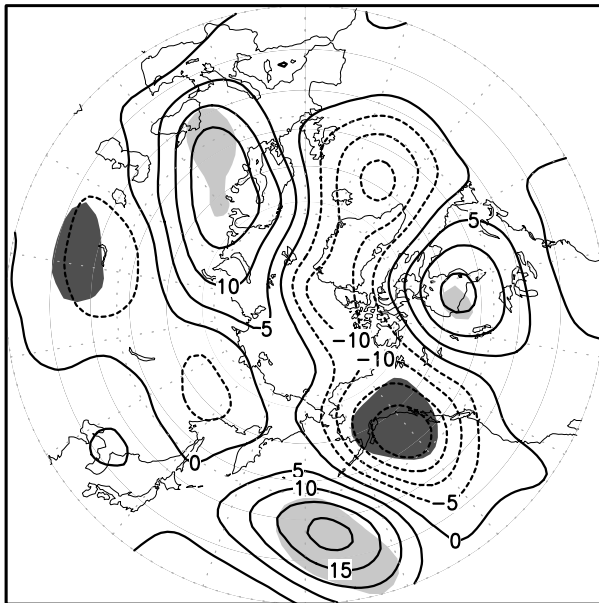


FIG. 9. Regression map between September–October 500-hPa geopotential height (m) and  $Q_{sfc}$  canonical correlation time series for CCA1. Light and dark shading indicates areas where the positive and negative correlation between them exceeds the 95% confidence level, respectively.

transport anomalies in the Bering Strait in September–October, the positive ATW volume transport anomaly in 2016 becomes more prominent with a value of 0.34 Sv and the SIA in the Chukchi Sea also shows a minimum value (Fig. 12b). These results imply that the contribution of the ocean heat transport related to the Bering Strait volume transport to the ocean heat condition in the Chukchi Sea has become larger in recent years.

Earlier studies identified that the interannual variability of the volume transport in the Bering Strait induced by the sea level difference between the Pacific and Arctic Oceans is related to the Canada Basin (Beaufort high) and the Bering Sea (Aleutian low) (Danielson et al. 2014; Peralta-Ferriz and Woodgate 2017). Here, we explore the atmospheric circulation pattern responsible for the interannual variability of ATWs in September–October through regression onto the canonical correlation time series of CCA1 for the 2-month leading ADV. The map of regression of SLP in September–October onto the canonical correlation time series of ADV is shown in Fig. 13a. Significant positive and negative anomalies are found in the Canada Basin and east of the Kamchatka Peninsula, respectively. The correlation between the time series of CCA1 for ADV and SLP in the Canada Basin (77.5°N, 150°W) during the entire analyzed period is significant at the 95% confidence level ( $r = 0.46$ ), but the correlation between them becomes small after 2000 ( $r = 0.09$ ). The time series of SLP in the Canada Basin shows that year-to-year variability is prominent in autumn and that there are no noticeable linear trends (Fig. 13b), similar to the case of the summertime Beaufort high (Hori et al. 2015). Conversely, the

time series of SLP east of the Kamchatka Peninsula (65°N, 170°E) is highly correlated with the time series of CCA1 for ADV during the entire analyzed period ( $r = -0.49$ ) and the significant correlation between them persists after 2000 ( $r = -0.70$ ). This result is consistent with the findings of Serreze et al. (2019), showing that the wind-driven volume transport in the Bering Strait, based on mooring observations, is correlated significantly with SLP east of the Kamchatka Peninsula. It is noteworthy that the time series of SLP east of the Kamchatka Peninsula shows a weak trend of decrease with a minimum in 2016 (Fig. 13b). Thus, it is suggested that the interannual variability of ocean heat advection in the Chukchi Sea and the maximum ATW in 2016 were controlled by the volume transport in the Bering Strait driven by the southeasterly wind anomaly related to the low SLP anomaly east of the Kamchatka Peninsula rather than by the high SLP anomaly in the Canada Basin.

It is interesting to consider the cause of the anomalously low SLP east of the Kamchatka Peninsula in autumn 2016. Using the entire record of the A3 mooring observations, Serreze et al. (2019) discussed the importance of the low SLP east of the Kamchatka Peninsula in October 2016, which is related to the highest heat and volume transports in the Bering Strait, but the formation mechanism of the SLP anomaly has not been examined. The year 2016 was characterized by frequent occurrence of relatively strong tropical cyclones in autumn (JMA 2016). In particular, three large tropical cyclones migrated northward to reach northern Japan, where large amounts of rainfall influenced the land and ocean environments (Kuroda et al. 2020). Therefore, the northward migration of these tropical cyclones might have influenced wind conditions in the ESS. Examination of the NCEP–NCAR reanalysis monthly mean SLP data indicates that the anomalous low values occurred to the east of the Kamchatka Peninsula in September–October 2016 (Fig. 14a). Examination of the daily mean SLP indicates that the anomalous low signal of SLP was partly related to the northward migration of a long-lived category-5 tropical cyclone (TC Chaba). This tropical cyclone was generated on September 26, and it moved northward to the east of the Kamchatka Peninsula by 6 October, strengthening along the way (Fig. 14a). In association with the cyclonic circulation to the east of the Kamchatka Peninsula, strong easterly winds occurred over the ESS on 7 October. The time series of mean SLP to the east of the Kamchatka Peninsula shows that SLP reached 990 hPa around 6 October (Fig. 14b), and the zonal wind speed shows a strong easterly wind of  $\sim 10 \text{ m s}^{-1}$  (Fig. 14c), which is suitable for the generation of ATWs in the ESS. These results demonstrate that the anomalously low SLP to the east of the Kamchatka Peninsula in September–October 2016 and the enhancement of ATWs are highly influenced by the northward migration of tropical cyclones.

## 7. Summary and discussion

In this study, we investigated the seasonal predictability of sea ice advance in the Chukchi Sea in early winter through statistical analysis of long-term ice–ocean coupled reanalysis data, which realistically reproduce the year-to-year variability

## Canonical correlation maps

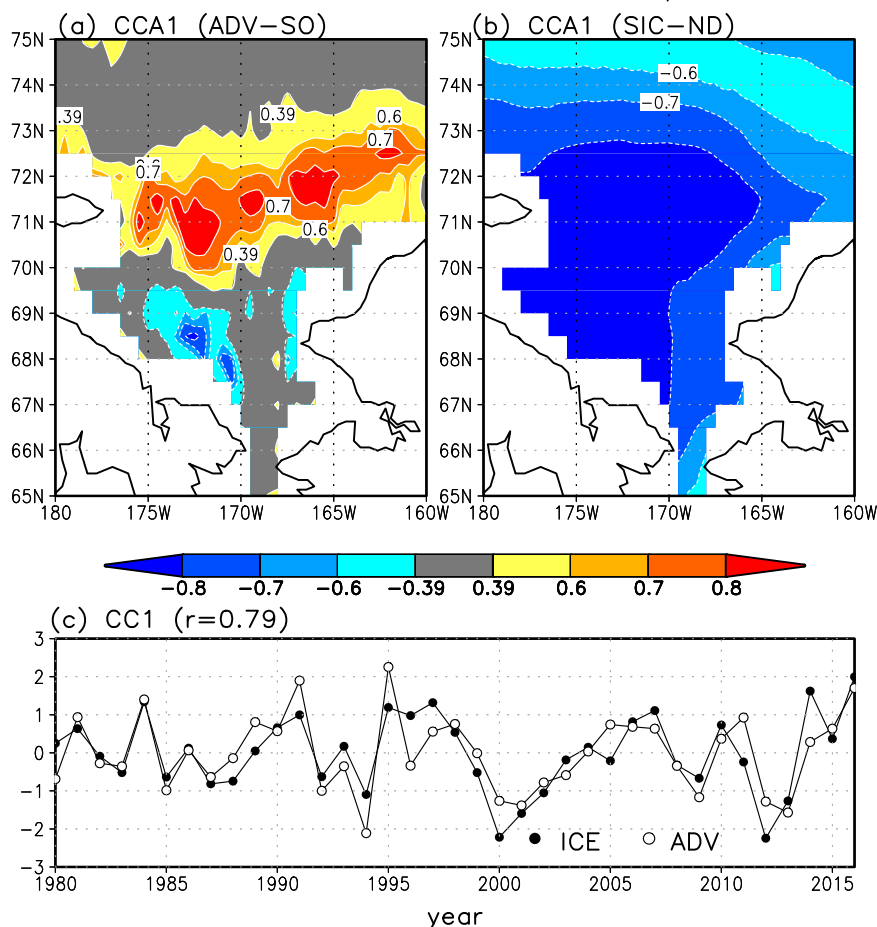


FIG. 10. CCA mode 1 of the 2-month leading ADV predictor case. Canonical correlation map of (a) ADV (September–October) and (b) SIC (November–December), and (c) time series of canonical correlation for ADV and SIC. The canonical correlation between them is 0.79. Colored regions in (a) and (b) indicate areas where the correlations are significant at the 95% confidence level.

of the ice–ocean fields in and around the Chukchi Sea. We found that the 2-month leading (September–October; autumn) ocean HC from 0- to 50-m depth in the Chukchi Sea is the main factor for the interannual variability of sea ice advance through change in the sea ice production process. The ocean HC responsible for SIC predictability is independently related to surface heat flux and ocean heat advection. Our objective analysis based on PIOMAS outputs confirms that Bering Strait heat transport in summer–autumn is the dominant predictor for the timing of sea ice advance in the Chukchi Sea (Serreze et al. 2016).

Upward surface heat flux, which is related to cooling by northeasterly winds, enhances sea ice advance in the south-eastern Chukchi Sea. Sea ice advance was prominent in the 1980s to 1990s, which was related to this surface cooling process by anomalous northeasterly winds. The northeasterly wind anomalies in these years were related to the east Pacific–North Pacific teleconnection pattern. Nakanowatari et al. (2015) identified the connection between the interannual

variability of the sea ice area in the Bering Sea and the summertime atmosphere teleconnection pattern, which is related to atmospheric convection in the western tropical Pacific Ocean. Yuan and Xiao (2018) reported significant connection between SST fluctuation in the Kuroshio–Oyashio confluence and surface air temperature in the western and eastern North Pacific through the meandering of the westerlies. Therefore, the east Pacific–North Pacific teleconnection pattern related to the northeasterly wind might be linked to air–sea interactions in the northwestern Pacific.

Ocean heat advection within the Chukchi Sea, which is controlled by the strength of the volume transport in the Bering Strait, has a role in suppressing sea ice advance in the northwestern Chukchi Sea. The strength of the autumn volume transport in the Bering Strait is related to SSH variability in the ESS, which is well explained by the ATWs forced by southeasterly wind stress along the shelf of the ESS. The importance of sea level variability on the pressure head driving force for the volume transport in the Bering Strait has



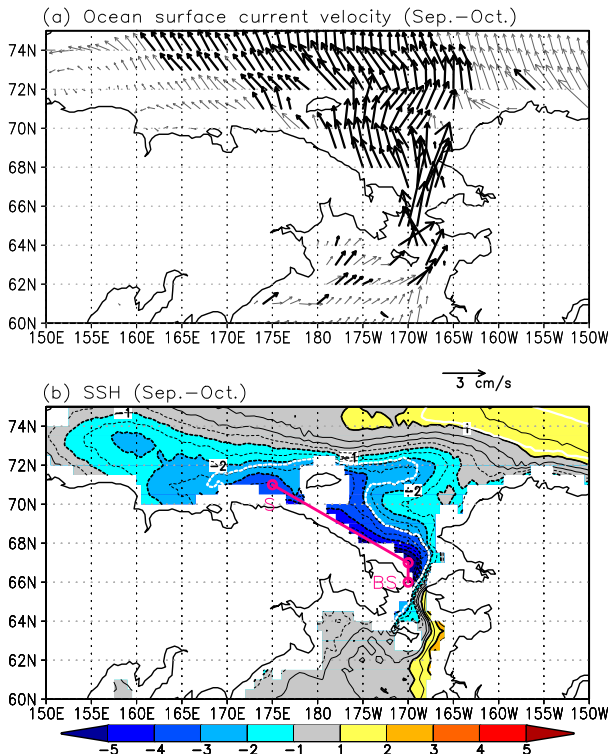


FIG. 11. Regression map of (a) surface ocean current anomaly ( $\text{cm s}^{-1}$ ; vectors) and (b) SSH anomaly (cm; colors) in September–October onto the canonical correlation time series for ADV from 1980 to 2016. In (a) and (b), the surface ocean current and SSH anomalies, for which the correlations are significant at the 95% confidence level, are shown by bold vectors (black) and contours (white), respectively. In (b), the integral routes of ATWs are defined by the magenta line from the start point (S) to the Bering Strait (BS).

been identified in earlier studies (e.g., [Peralta-Ferriz and Woodgate 2017](#)), but application of ATW theory to the volume transport in the Bering Strait and its quantitative evaluation is a new finding. Our study also found that a possible cause of the wind stress is the SLP anomaly east of the Kamchatka Peninsula rather than the high pressure system in the Canada Basin. In particular, the anomalously low sea ice in 2016 was partly caused by abnormal ATWs driven by strong southeasterly winds associated with northward migration of a tropical cyclone. It has been reported that a poleward trend of tropical cyclone migration has been evident in both hemispheres since the 1980s ([Kossin et al. 2014](#)). Moreover, the number of tropical cyclones in the western North Pacific has increased since 1980 ([Yamaguchi and Maeda 2020](#)). Thus, the wind-driven process of ocean heat advection would likely exacerbate the delay of sea ice advance in early winter caused by the ocean and atmosphere warming projected in the future.

During 2014–16, unusually warm ocean temperatures occurred in the southeastern Bering Sea, associated with strong advection of warm water from the Gulf of Alaska through the Unimak Pass ([Stabeno et al. 2017](#)). Moreover, it

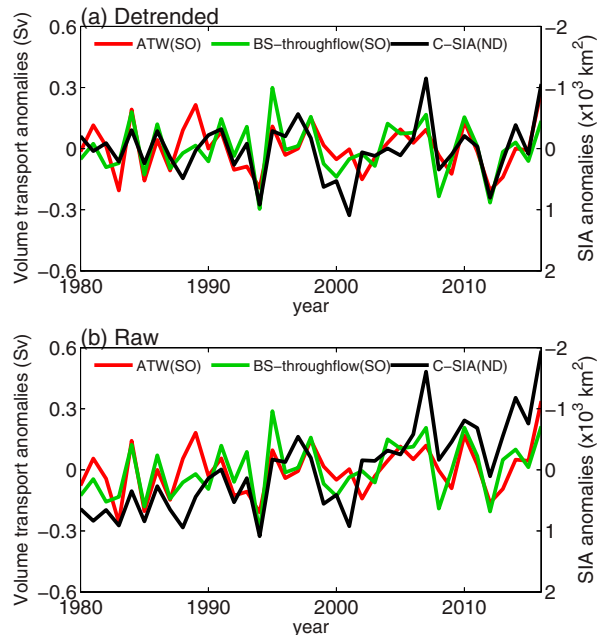


FIG. 12. (a) Time series of the autumn (September–October) ATW transport anomalies (red) in the Bering Strait (BS) (shown in [Fig. 11](#)), volume transport in the BS from PIOMAS (green), and SIA anomalies in the Chukchi Sea (black) from 1980 to 2016 without the linear trend component. (b) As in (a), but for the raw monthly mean data with the linear trend component. The scale of the SIA anomalies is shown on the right-hand axis and inverted for comparison with the volume transport.

was also reported that an unprecedented warming event occurred in the Gulf of Alaska and the Bering Sea in 2016, which reflected the combination of a strong El Niño event with a positive phase of the Pacific decadal oscillation and anomalous deepening of the Aleutian low ([Walsh et al. 2018](#)). Because some of the warm water in the Bering Sea flows into the Chukchi Sea through the Bering Strait, the 2016 delay of sea ice advance in early winter was also influenced by this

TABLE 2. Correlation coefficients between the time series of ATWs along the East Siberian Sea calculated from the wind stress from the NCEP–NCAR reanalysis and ERA-Interim, the SIA in the Chukchi Sea in November–December, and the Bering Strait (BS) volume transport derived from PIOMAS outputs in September–October. Bold numbers indicate correlations exceeding the 95% confidence level based on the Monte Carlo simulation, using a phase randomization technique generating 1000 surrogate time series ([Kaplan and Glass 1995](#)).

	SIA (1980–2016)	BS volume transport (1980–2016)	SIA (2001–16)
ATW (NCEP–NCAR)	<b>−0.55</b>	<b>0.69</b>	<b>−0.63</b>
ATW (ERA-Interim)	<b>−0.54</b>	<b>0.69</b>	<b>−0.69</b>

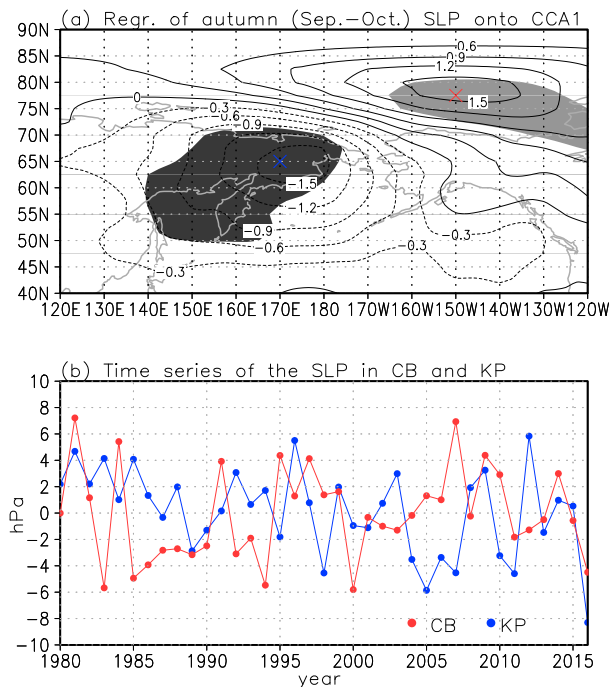


FIG. 13. (a) Regression map (contours) of monthly mean SLP (hPa) in September–October onto the canonical correlation time series of ADV. Shadings indicate significance at the 95% confidence level. (b) Time series of monthly mean SLP anomalies in the Canada Basin [CB; 77.5°N, 150°W, marked by the red cross in (a)] and east of the Kamchatka Peninsula (KP; 65°N, 170°E, marked by the blue cross) in September–October.

warm water advection. Kodaira et al. (2020) reported that water temperature was anomalously warm and there was less sea ice in the Chukchi Sea in 2018–20. They highlighted that a distinct southerly wind related to an atmospheric blocking high system over the Bering Sea induces wind-driven transport in the Bering Strait. Thus, for precise forecasting of sea ice advance in the Chukchi Sea, further investigation of the upstream ocean thermal conditions and wind-driven ocean current system responsible for the volume transport in the Bering Strait must be conducted.

Lenetsky et al. (2021) examined the interannual variability of ocean heat transport using long-term mooring observations from the Bering Strait for 1998–2015. They revealed the importance of the ocean temperature anomaly to ocean heat transport and skillful prediction of sea ice advance in the Chukchi Sea. Although we focused on the importance of the volume transport change in the Bering Strait with regard to ocean heat advection in the Chukchi Sea, we also obtained the highest prediction skill of SIC in the Chukchi Sea, when the 2-month leading ocean HC was used for the predictor (Fig. 4), which is consistent with their study. The ocean temperature anomaly is determined by surface heat flux as well as by lateral advection anomalies; therefore, the ocean temperature signal is considered a better predictor for sea ice advance in the Chukchi Sea.

Although the variability of sea ice advance is determined by atmospheric cooling (promotion effect) and ocean heat

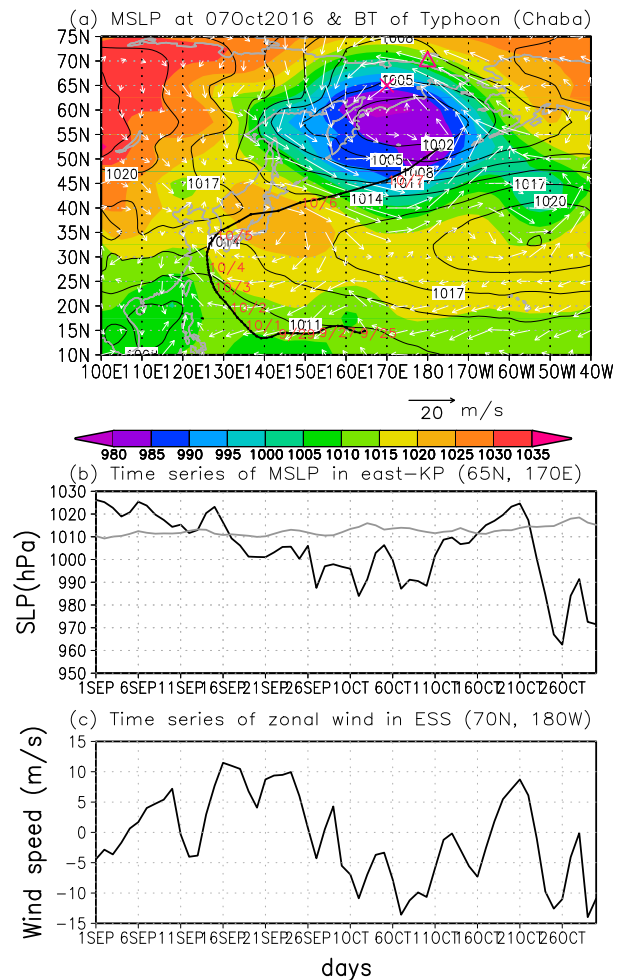


FIG. 14. (a) Daily mean SLP distribution (hPa; colors) and surface wind speed ( $\text{m s}^{-1}$ ; vectors) on 7 Oct 2016, and the tracking route for TC Chaba (black line). The location of the center of the typhoon is plotted with the arrival date (red). The monthly mean SLP (hPa) averaged in September–October 2016 is also indicated by contours (thin black). (b) Time series of the daily mean SLP east of the Kamchatka Peninsula [KP; 65°N, 170°E, shown in (a) by the cross] from 1 Sep to 30 Oct 2016 (black) and its climatology (gray). (c) As in (b), but for the zonal wind speed ( $\text{m s}^{-1}$ ) in the East Siberian Sea [EES; 70°N, 180°W, marked by the triangle in (a)].

advection (suppression effect), there is a possibility that the dominant mechanism has shifted from an atmospheric process to an oceanic process since the 2000s. In fact, we established that the interannual variability of SIA in the Chukchi Sea has been sensitive to that of ATWs after 2000. The comparison between the canonical correlation time series for CCA1 for ADV and  $Q_{\text{sfc}}$  in September–October and SIA in the Chukchi Sea also supports the above hypothesis (Fig. 15). The correlation between the canonical correlation time series of  $Q_{\text{sfc}}$  and SIA is significant before 2000 ( $r = -0.71$ ), but their correlation is small after 2000 ( $r = -0.08$ ). Conversely, the canonical correlation time series of ADV is correlated significantly with SIA in the Chukchi Sea during the entire analyzed

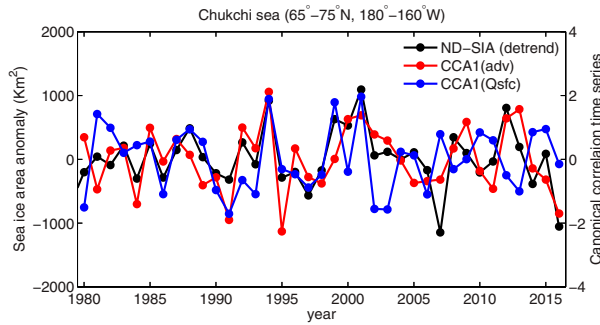


FIG. 15. Time series of the detrended SIA averaged over the Chukchi Sea ( $65^{\circ}$ – $75^{\circ}$ N,  $180^{\circ}$ – $160^{\circ}$ W; black) in November–December and the canonical correlation time series of ADV (red) and  $Q_{sfc}$  (blue) in September–October. The scale of the canonical correlation time series is shown on the right-hand axis.

period ( $r = 0.67$ ), including the period after 2000 ( $r = 0.63$ ). Because SIA has decreased drastically since the 2000s (Fig. 1b), the ocean temperature in the Chukchi Sea might not be effectively cooled, even under northeasterly wind conditions. CMIP6 multimodel ensemble forecasts under global warming scenario SSP2–4.5 or SSP5–8.5 (Notz et al. 2020) project that the Arctic Ocean will become practically free of sea ice in September before the middle of the twenty-first century; therefore, it is suggested that ocean heat advection could become a principal influencing factor of the interannual variability of sea ice advance in the Chukchi Sea in the future.

Oceanographic in situ observations are very limited in polar regions, and the resultant data gap limits the reliability of ocean and sea ice forecasts (Smith et al. 2019). Toward improvement of weather and climate predictions in the Arctic region, the optimum observing system in the Arctic region and effective exploitation of current observations in numerical weather and climate forecast systems have been discussed within the framework of international research projects such as the Polar Prediction Project of the World Meteorological Organization. The findings of our study indicate that autumn preconditioning of ocean heat conditions in the Chukchi Sea, which is related to ocean heat advection from the Bering Strait, has made a large contribution to the interannual variability of the sea ice advance in early winter since the 2000s. Therefore, development of a pan-Arctic near-real-time observing system using Argo profiling floats and expansion of the voluntary observing ship program will be necessary for enhanced skill in predicting sea ice in the marginal sea ice zone through improvement of the initial conditions of forecast models. Because this study was based on a statistical examination using hindcast outputs, to design a pan-Arctic near-real-time observing system, we will need to examine the impact of enhanced in situ observations on sea ice forecast skill using an ice–ocean coupled data assimilation system.

**Acknowledgments.** We thank R. Woodgate of the University of Washington for providing the mooring observational dataset for the period 1990–2016. We wish to thank M. Steele and R. Woodgate of the University of

Washington, Y. Kawaguchi of the University of Tokyo, M. Itoh, S. Nishino, T. Kikuchi of JAMSTEC, F. Massonnet of UCLouvain, and the two anonymous reviewers for their insightful constructive comments and fruitful discussions. A number of figures were produced using the GrADS package developed by B. Doty. This work was supported by JSPS KAKENHI (18H03745, 24241009, 17KK0014) and the Arctic Challenge for Sustainability (ArCS) and ArCS II projects of the Ministry of Education, Culture, Sports, Science and Technology in Japan. J.Z. was supported by the NSF Office of Polar Programs (PLR-1603259, PLR-1602985, and NNA-1927785) and the NASA Cryosphere Program (NNX17AD27G). We thank James Buxton, MSc, from Edanz (<https://jp.edanz.com/ac>) for editing a draft of this manuscript. The PIOMAS data are available on the web site for the Polar Science Center, the University of Washington ([http://psc.apl.uw.edu/research/projects/arctic-sea-ice-volume-anomaly/data/model\\_grid](http://psc.apl.uw.edu/research/projects/arctic-sea-ice-volume-anomaly/data/model_grid)). The A3 mooring observational dataset is available on the web site for the Polar Science Center, the University of Washington (<http://psc.apl.washington.edu/HLD/Bstrait/Data/BeringStraitMooringDataArchive.html>). Sea ice concentration data are openly available from the NASA National Snow and Ice Data Center Distributed Active Archive Center [<https://doi.org/10.5067/8GQ8LZQVL0VL>] as cited in Cavalieri et al. (1996). The NCEP–NCAR reanalysis data are available from the website for the NOAA Physical Science Laboratory (<https://psl.noaa.gov/data/gridded/data.ncep.reanalysis.html>). The ERA-Interim data are publicly available from the ECMWF portal site (<https://www.ecmwf.int/en/forecasts/datasets/reanalysis-datasets/era-interim>). The tracking data for Tropical Cyclone are available from the web site for the Regional Specialized Meteorological Center (RSMC) Tokyo–Typhoon Center ([https://www.jma.go.jp/jma/jma-eng/jma-center/rsmc-hp-pub-eg/RSMC\\_HP.htm](https://www.jma.go.jp/jma/jma-eng/jma-center/rsmc-hp-pub-eg/RSMC_HP.htm)).

## APPENDIX

### Canonical Correlation Analysis

This appendix provides a mathematical expression of the CCA methodology used in this study. In accordance with Barnett and Preisendorfer (1987), the two-dimensional predictand  $T(x', t)$  and predictor data  $Y(x, t)$  are standardized by and prefiltered with PCA as follows:

$$Y(x, t) = \sum_{j=1}^p \kappa_j^{1/2} \alpha_j(t) e_j(x), \quad x = 1, 2, \dots, p, \quad (A1)$$

$$T(x', t) = \sum_{j=1}^q \lambda_j^{1/2} \beta_j(t) f_j(x'), \quad x' = 1, 2, \dots, q,$$

where  $\kappa_j$  and  $\lambda_j$  are the eigenvalues,  $\alpha_j(t)$  and  $\beta_j(t)$  are the principal components, and  $e$  and  $f$  are the eigenvectors for EOF mode  $j$ . The truncation modes  $p$  and  $q$  are determined by the truncation rule of the principal components based on the Monte Carlo technique with 100 surrogate data points with temporal variations of white noise.

From the truncated principal components, the cross-correlation matrix  $\mathbf{C}$  ( $p \times q$ ) is calculated as follows:

$$c_{jk} = \langle \alpha_j(t) \beta_k(t) \rangle_t, \quad (\text{A2})$$

where angle brackets ( $\langle \rangle$ ) denote an average over time. The canonical component vectors ( $u_j$  and  $v_k$ ) are estimated by solving the eigenvalue problems of matrix  $C_{jk}$ :

$$\left. \begin{aligned} [\mathbf{C}\mathbf{C}^T]\mathbf{r}_j &= \mu_j^2 \mathbf{r}_j, \quad j = 1, 2, \dots, p \\ [\mathbf{C}^T\mathbf{C}]\mathbf{s}_k &= \mu_k^2 \mathbf{s}_k, \quad k = 1, 2, \dots, q \end{aligned} \right\}, \quad (\text{A3})$$

where  $\mathbf{r}_j$  and  $\mathbf{s}_k$  are eigenvectors of matrix  $\mathbf{C}$ , which evaluate the contribution of each principal component  $\alpha_j(t)$  and  $\beta_j(t)$  to the corresponding canonical component vectors. The canonical component vectors are expressed as follows:

$$u_j = \sum_{i=1}^p \alpha_i r_{ij} \quad \text{and} \quad v_k = \sum_{i=1}^q \beta_i s_{ik}. \quad (\text{A4})$$

They are also referred to the canonical correlation time series, and the correlations between the canonical component vectors are called the canonical correlation coefficients.

The canonical correlation maps ( $g_j$  and  $h_k$ ) for the predictor and the predictand are obtained by  $T(x', t)$  or  $Y(x, t)$  and the corresponding canonical component vectors:

$$g_j(x) = \langle Y(x, t) u_j(t) \rangle_t, \quad h_k(x') = \langle T(x', t) v_k(t) \rangle_t. \quad (\text{A5})$$

Finally, the predicted value ( $T'$ ) is estimated from the linear combination of the eigenvalue ( $\mu_j$ ), canonical correlation map ( $h_j$ ), and the canonical component vectors of  $u_j(t)$ :

$$T'(x', t) = \sum_{j=1}^{q''} \mu_j u_j(t) h_j(x'), \quad x' = 1, \dots, q'' \leq q. \quad (\text{A6})$$

The adopted CCA modes ( $q''$ ) for the prediction, determined by the statistical significance test, are usually equal to or less than the total CCA modes ( $q$ ).

## REFERENCES

- Barnett, T. P., and R. Preisendorfer, 1987: Origins and levels of monthly and seasonal forecast skill for United States surface air temperatures determined by canonical correlation analysis. *Mon. Wea. Rev.*, **115**, 1825–1850, [https://doi.org/10.1175/1520-0493\(1987\)115<1825:OALOMA>2.0.CO;2](https://doi.org/10.1175/1520-0493(1987)115<1825:OALOMA>2.0.CO;2).
- Barnston, A. G., 1994: Linear short-term climate predictive skill in the Northern Hemisphere. *J. Climate*, **7**, 1513–1564, [https://doi.org/10.1175/1520-0442\(1994\)007<1513:LSSTCP>2.0.CO;2](https://doi.org/10.1175/1520-0442(1994)007<1513:LSSTCP>2.0.CO;2).
- , and R. E. Livezey, 1987: Classifications, seasonality, and persistence of low-frequency atmospheric circulation patterns. *Mon. Wea. Rev.*, **115**, 1083–1126, [https://doi.org/10.1175/1520-0493\(1987\)115<1083:CSAPOL>2.0.CO;2](https://doi.org/10.1175/1520-0493(1987)115<1083:CSAPOL>2.0.CO;2).
- Bonan, D. B., M. Bushuk, and M. Winton, 2019: A spring barrier for regional predictions of summer Arctic sea ice. *Geophys. Res. Lett.*, **46**, 5937–5947, <https://doi.org/10.1029/2019GL082947>.
- Bretherton, C. S., C. Smith, and J. M. Wallace, 1992: An inter-comparison of methods for finding coupled patterns in climate data. *J. Climate*, **5**, 541–560, [https://doi.org/10.1175/1520-0442\(1992\)005<0541:AIOMFF>2.0.CO;2](https://doi.org/10.1175/1520-0442(1992)005<0541:AIOMFF>2.0.CO;2).
- Brodzik, M. J., and J. S. Stewart, 2016: Near-Real-Time SSM/I-SSMIS EASE-Grid Daily Global Ice. National Snow and Ice Data Center Distributed Active Archive Center, accessed 18 July 2017, <https://doi.org/10.5067/3KB2JPLFPK3R>.
- Bushuk, M., M. Winton, D. B. Bonan, E. Blanchard-Wrigglesworth, and T. L. Delworth, 2020: A mechanism for the Arctic sea ice spring predictability barrier. *Geophys. Res. Lett.*, **47**, e2020GL088335, <https://doi.org/10.1029/2020GL088335>.
- Cavalieri, D. J., and C. L. Parkinson, 2012: Arctic sea ice variability and trends, 1979–2010. *Cryosphere*, **6**, 881–889, <https://doi.org/10.5194/tc-6-881-2012>.
- , —, P. Gloersen, and H. J. Zwally, 1996: Sea Ice Concentrations from Nimbus-7 SMMR and DMSP SSM/I-SSMIS Passive Microwave Data, Version 1; 1979–2016. NASA National Snow and Ice Data Center Distributed Active Archive Center, accessed 2 July 2020, <https://doi.org/10.5067/8GQ8LZQVLOVL>.
- Chen, J., and Coauthors, 2020: Changes in sea ice and future accessibility along the Arctic Northeast Passage. *Global Planet. Change*, **195**, 103319, <https://doi.org/10.1016/j.gloplacha.2020.103319>.
- Csanady, G. T., 1978: The arrested topography wave. *J. Phys. Oceanogr.*, **8**, 47–62, [https://doi.org/10.1175/1520-0485\(1978\)008<0047:TATW>2.0.CO;2](https://doi.org/10.1175/1520-0485(1978)008<0047:TATW>2.0.CO;2).
- Danielson, S. L., T. J. Weingartner, K. S. Hedstrom, K. Aagaard, R. Woodgate, E. Curchitser, and P. J. Staben, 2014: Coupled wind-forced controls of the Bering–Chukchi shelf circulation and the Bering Strait throughflow: Ekman transport, continental shelf waves, and variations of the Pacific–Arctic sea surface height gradient. *Prog. Oceanogr.*, **125**, 40–61, <https://doi.org/10.1016/j.pocan.2014.04.006>.
- Dee, D. P., and Coauthors, 2011: The ERA-Interim reanalysis: Configuration and performance of the data assimilation system. *Quart. J. Roy. Meteor. Soc.*, **137**, 553–597, <https://doi.org/10.1002/qj.828>.
- De Silva, L. W. A., J. Inoue, H. Yamaguchi, and T. Terui, 2020: Medium range sea ice prediction in support of Japanese research vessel MIRAI's expedition cruise in 2018. *Polar Geogr.*, **43**, 223–239, <https://doi.org/10.1080/1088937X.2019.1707317>.
- Eguíluz, V. M., J. Fernández-Gracia, X. Irigoien, and C. M. Duarte, 2016: A quantitative assessment of Arctic shipping in 2010–2014. *Sci. Rep.*, **6**, 30682, <https://doi.org/10.1038/srep30682>.
- Elsner, J. B., and C. P. Schmertmann, 1994: Assessing forecast skill through cross validation. *Wea. Forecasting*, **9**, 619–624, [https://doi.org/10.1175/1520-0434\(1994\)009<0619:AFSTCV>2.0.CO;2](https://doi.org/10.1175/1520-0434(1994)009<0619:AFSTCV>2.0.CO;2).
- Grebmeier, J. M., and W. Maslowski, 2014: *The Pacific Arctic Region: Ecosystem Status and Trends in a Rapidly Changing Environment*. Springer, 450 pp.
- , and Coauthors, 2006: A major ecosystem shift in the northern Bering Sea. *Science*, **311**, 1461–1464, <https://doi.org/10.1126/science.1121365>.
- Hori, M., J. Inoue, and T. Kikuchi, 2015: The role of cyclone activity in the interannual variability of the summertime Beaufort high. *SOLA*, **11**, 104–107, <https://doi.org/10.2151/sola.2015-025>.
- Hunt, G. L., Jr., and Coauthors, 2013: The Barents and Chukchi Seas: Comparison of two Arctic shelf ecosystems. *J. Mar.*



- Syst.*, **109**–**110**, 43–68, <https://doi.org/10.1016/j.jmarsys.2012.08.003>.
- Inoue, J., T. Enomoto, T. Miyoshi, and S. Yamane, 2009: Impact of observations from Arctic drifting buoys on the reanalysis of surface fields. *Geophys. Res. Lett.*, **36**, L08501, <https://doi.org/10.1029/2009GL037380>.
- JMA, 2016: Climate change monitoring report. Japan Meteorological Agency, 92 pp., [https://www.jma.go.jp/jma/en/NMHS/ccmr/ccmr2016\\_high.pdf](https://www.jma.go.jp/jma/en/NMHS/ccmr/ccmr2016_high.pdf).
- Kalnay, E., and Coauthors, 1996: The NCEP/NCAR 40-Year Reanalysis Project. *Bull. Amer. Meteor. Soc.*, **77**, 437–471, [https://doi.org/10.1175/1520-0477\(1996\)077<0437:TNYRP>2.0.CO;2](https://doi.org/10.1175/1520-0477(1996)077<0437:TNYRP>2.0.CO;2).
- Kaplan, D., and L. Glass, 1995: *Understanding Nonlinear Dynamics*. Springer-Verlag, 420 pp.
- Kawaguchi, Y., and Coauthors, 2020: Cold water upwelling near the Anadyr Strait: Observations and simulations. *J. Geophys. Res. Oceans*, **125**, e2020JC016238, <https://doi.org/10.1029/2020JC016238>.
- Kodaira, T., T. Waseda, T. Nose, and J. Inoue, 2020: Record high Pacific Arctic seawater temperatures and delayed sea ice advance in response to episodic atmospheric blocking. *Sci. Rep.*, **10**, 20830, <https://doi.org/10.1038/s41598-020-77488-y>.
- Kossin, J. P., K. A. Emanuel, and G. A. Vecchi, 2014: The poleward migration of the location of tropical cyclone maximum intensity. *Nature*, **509**, 349–352, <https://doi.org/10.1038/nature13278>.
- Koyama, T., T. Nakanowatari, and J. Inoue, 2021: Information retrieval for Northern Sea Route (NSR) navigation: A statistical approach using the AIS and TOPAZ4 data. *Polar Sci.*, **27**, 100626, <https://doi.org/10.1016/j.polar.2020.100626>.
- Kug, J. S., J.-H. Jeong, Y.-S. Jang, B.-M. Kim, C. K. Folland, S.-K. Min, and S.-W. Son, 2015: Two distinct influences of Arctic warming on cold winters over North America and East Asia. *Nat. Geosci.*, **8**, 759–762, <https://doi.org/10.1038/ngeo2517>.
- Kuroda, H., T. Saito, T. Kaga, A. Takasuka, Y. Kamimura, S. Furuichi, and T. Nakanowatari, 2020: Unconventional sea surface temperature regime around Japan in the 2000s–2010s: Potential influences on major fisheries resources. *Front. Mar. Sci.*, **7**, 574904, <https://doi.org/10.3389/fmars.2020.574904>.
- Lee, M.-Y., C.-C. Hong, and H.-H. Hsu, 2015: Compounding effects of warm sea surface temperature and reduced sea ice on the extreme circulation over the extratropical North Pacific and North America during the 2013–2014 boreal winter. *Geophys. Res. Lett.*, **42**, 1612–1618, <https://doi.org/10.1002/2014GL062956>.
- Lenetsky, J. E., and M. C. Serreze, 2021: Statistical modeling of the Bering Strait throughflow for operational sea ice forecasting in the Chukchi Sea. *Geophys. Res. Lett.*, **48**, e2021GL092939, <https://doi.org/10.1029/2021GL092939>.
- , B. Tremblay, C. Brunette, and G. Meneghello, 2021: Subseasonal predictability of Arctic Ocean sea ice conditions: Bering Strait and Ekman-driven ocean heat transport. *J. Climate*, **34**, 4449–4462, <https://doi.org/10.1175/JCLI-D-20-0544.1>.
- Leppäranta, M., 2005: *The Drift of Sea Ice*. Springer, 350 pp.
- Melia, N., K. Haines, and E. Hawkins, 2016: Sea ice decline and 21st century trans-Arctic shipping routes. *Geophys. Res. Lett.*, **43**, 9720–9728, <https://doi.org/10.1002/2016GL069315>.
- Michaelsen, J., 1987: Cross-validation in statistical climate forecast models. *J. Climate Appl. Meteor.*, **26**, 1589–1600, [https://doi.org/10.1175/1520-0450\(1987\)026<1589:CVISCF>2.0.CO;2](https://doi.org/10.1175/1520-0450(1987)026<1589:CVISCF>2.0.CO;2).
- Nakanowatari, T., and K. I. Ohshima, 2014: Coherent sea level variation in and around the Sea of Okhotsk. *Prog. Oceanogr.*, **126**, 58–70, <https://doi.org/10.1016/j.pocean.2014.05.009>.
- , K. Sato, and J. Inoue, 2014: Predictability of the Barents Sea ice in early winter: Remote effects of oceanic and atmospheric thermal conditions from the North Atlantic. *J. Climate*, **27**, 8884–8901, <https://doi.org/10.1175/JCLI-D-14-00125.1>.
- , J. Inoue, K. Sato, and T. Kikuchi, 2015: Summertime atmosphere–ocean preconditionings for the Bering Sea ice retreat and the following severe winters in North America. *Environ. Res. Lett.*, **10**, 094023, <https://doi.org/10.1088/1748-9326/10/9/094023>.
- NOAA/CPC, 2021: Northern Hemisphere Teleconnection Patterns: Historical Index Time Series. NOAA/Climate Prediction Center, accessed 1 July 2021, <https://www.cpc.ncep.noaa.gov/data/teledoc/telecontents.shtml>.
- Nose, T., A. Webb, T. Waseda, J. Inoue, and K. Sato, 2018: Predictability of storm wave heights in the ice-free Beaufort Sea. *Ocean Dyn.*, **68**, 1383–1402, <https://doi.org/10.1007/s10236-018-1194-0>.
- Notz, D., and Coauthors, 2020: Arctic sea ice in CMIP6. *Geophys. Res. Lett.*, **47**, e2019GL086749, <https://doi.org/10.1029/2019GL086749>.
- Overland, J. E., 2020: Less climatic resilience in the Arctic. *Wear. Climate Extremes*, **30**, 100275, <https://doi.org/10.1016/j.wace.2020.100275>.
- , and C. H. Pease, 1982: Cyclone climatology of the Bering Sea and its relation to sea ice extent. *Mon. Wea. Rev.*, **110**, 5–13, [https://doi.org/10.1175/1520-0493\(1982\)110<0005:CCOTBS>2.0.CO;2](https://doi.org/10.1175/1520-0493(1982)110<0005:CCOTBS>2.0.CO;2).
- Parkinson, C. L., and W. M. Washington, 1979: A large-scale numerical model of sea ice. *J. Geophys. Res.*, **84**, 311–337, <https://doi.org/10.1029/JC084iC01p00311>.
- , and J. C. Comiso, 2013: On the 2012 record low Arctic sea ice cover: Combined impact of preconditioning and an August storm. *Geophys. Res. Lett.*, **40**, 1356–1361, <https://doi.org/10.1002/grl.50349>.
- Peralta-Ferriz, C., and R. A. Woodgate, 2017: The dominant role of the East Siberian Sea in driving the oceanic flow through the Bering Strait: Conclusions from GRACE ocean mass satellite data and in situ mooring observations between 2002 and 2016. *Geophys. Res. Lett.*, **44**, 11 472–11 481, <https://doi.org/10.1002/2017GL075179>.
- Qiu, B., 2002: Large-scale variability in the mid-latitude subtropical and subpolar North Pacific Ocean: Observations and causes. *J. Phys. Oceanogr.*, **32**, 353–375, [https://doi.org/10.1175/1520-0485\(2002\)032<0353:LSVITM>2.0.CO;2](https://doi.org/10.1175/1520-0485(2002)032<0353:LSVITM>2.0.CO;2).
- Reynolds, R. W., T. M. Smith, C. Liu, D. B. Chelton, K. S. Casey, and M. G. Schlax, 2007: Daily high-resolution-blended analyses for sea surface temperature. *J. Climate*, **20**, 5473–5496, <https://doi.org/10.1175/2007JCLI1824.1>.
- Sasaki, Y. N., and S. Minobe, 2005: Seasonally dependent interannual variability of sea ice in the Bering Sea and its relation to atmospheric fluctuations. *J. Geophys. Res.*, **110**, C05011, <https://doi.org/10.1029/2004JC002486>.
- Schøyen, H., and S. Bråthen, 2011: The Northern Sea Route versus the Suez Canal: Cases from bulk shipping. *J. Transp. Geogr.*, **19**, 977–983, <https://doi.org/10.1016/j.jtrangeo.2011.03.003>.
- Schweiger, A., R. W. Lindsay, J. Zhang, M. Steele, H. Stern, and R. Kwok, 2011: Uncertainty in modeled Arctic sea ice volume. *J. Geophys. Res.*, **116**, C00D06, <https://doi.org/10.1029/2011JC007084>.

- Screen, J. A., 2017: Simulated atmospheric response to regional and pan-Arctic sea ice loss. *J. Climate*, **30**, 3945–3962, <https://doi.org/10.1175/JCLI-D-16-0197.1>.
- Serreze, M. C., and Coauthors, 2006: The large-scale freshwater cycle of the Arctic. *J. Geophys. Res.*, **111**, C111010, <https://doi.org/10.1029/2005JC003424>.
- , A. D. Crawford, J. C. Stroeve, A. P. Barrett, and R. A. Woodgate, 2016: Variability, trends, and predictability of seasonal sea ice retreat and advance in the Chukchi Sea. *J. Geophys. Res. Oceans*, **121**, 7308–7325, <https://doi.org/10.1002/2016JC011977>.
- , A. P. Barrett, A. D. Crawford, and R. A. Woodgate, 2019: Monthly variability in Bering Strait oceanic volume and heat transports, links to atmospheric circulation and ocean temperature, and implications for sea ice conditions. *J. Geophys. Res. Oceans*, **124**, 9317–9337, <https://doi.org/10.1029/2019JC015422>.
- Smedsrud, L. H., and Coauthors, 2013: The role of the Barents Sea in the Arctic climate system. *Rev. Geophys.*, **51**, 415–449, <https://doi.org/10.1002/rog.20017>.
- Smith, G. C., and Coauthors, 2019: Polar ocean observations: A critical gap in the observing system and its effect on environmental predictions from hours to a season. *Front. Mar. Sci.*, **6**, 429, <https://doi.org/10.3389/fmars.2019.00429>.
- Smith, R. D., J. K. Dukowicz, and R. C. Malone, 1992: Parallel ocean general circulation modeling. *Physica D*, **60**, 38–61, [https://doi.org/10.1016/0167-2789\(92\)90225-C](https://doi.org/10.1016/0167-2789(92)90225-C).
- Springer, A. M., and C. P. McRoy, 1993: The paradox of pelagic food webs in the northern Bering Sea—III. Patterns of primary production. *Cont. Shelf Res.*, **13**, 575–599, [https://doi.org/10.1016/0278-4343\(93\)90095-F](https://doi.org/10.1016/0278-4343(93)90095-F).
- Stabeno, P. J., J. T. Duffy-Anderson, L. B. Eisner, E. V. Farley, R. A. Heintz, and C. W. Mordy, 2017: Return of warm conditions in the southeastern Bering Sea: Physics to fluorescence. *PLOS ONE*, **12**, e0185464, <https://doi.org/10.1371/journal.pone.0185464>.
- Stroeve, J., M. Serreze, S. Drobot, G. Gearheard, M. Holland, J. Maslanik, W. Meier, and T. Scambos, 2008: Arctic Sea ice extent plummets in 2007. *Eos, Trans. Amer. Geophys. Union*, **89**, 13–14, <https://doi.org/10.1029/2008EO020001>.
- Tachibana, Y., K. K. Komatsu, V. A. Alexeev, L. Cai, and Y. Ando, 2019: Warm hole in Pacific Arctic sea ice cover forced mid-latitude Northern Hemisphere cooling during winter 2017–18. *Sci. Rep.*, **9**, 5567, <https://doi.org/10.1038/s41598-019-41682-4>.
- Tivy, A., S. E. L. Howell, B. Alt, J. J. Yackel, and T. Carrieres, 2011: Origins and levels of seasonal forecast skill for sea ice in Hudson Bay using canonical correlation analysis. *J. Climate*, **24**, 1378–1395, <https://doi.org/10.1175/2010JCLI3527.1>.
- Walsh, J. E., and Coauthors, 2018: The high-latitude marine heat wave of 2016 and its impacts on Alaska. *Bull. Amer. Meteor. Soc.*, **99** (1), S39–S43, <https://doi.org/10.1175/BAMS-D-17-0105.1>.
- Woodgate, R. A., 2018: Increases in the Pacific inflow to the Arctic from 1990 to 2015, and insights into seasonal trends and driving mechanisms from year-round Bering Strait mooring data. *Prog. Oceanogr.*, **160**, 124–154, <https://doi.org/10.1016/j.pocean.2017.12.007>.
- , and C. Peralta-Ferriz, 2021: Warming and freshening of the Pacific inflow to the Arctic from 1990–2019 implying dramatic shoaling in Pacific Winter Water ventilation of the Arctic water column. *Geophys. Res. Lett.*, **48**, e2021GL092528, <https://doi.org/10.1029/2021GL092528>.
- , K. Aagaard, and T. J. Weingartner, 2005: Monthly temperature, salinity, and transport variability of the Bering Strait through flow. *Geophys. Res. Lett.*, **32**, L04601, <https://doi.org/10.1029/2004GL021880>.
- , —, and —, 2006: Interannual changes in the Bering Strait fluxes of volume, heat and freshwater between 1991 and 2004. *Geophys. Res. Lett.*, **33**, L15609, <https://doi.org/10.1029/2006GL026931>.
- , T. J. Weingartner, and R. Lindsay, 2010: The 2007 Bering Strait oceanic heat flux and anomalous Arctic sea ice retreat. *Geophys. Res. Lett.*, **37**, L01602, <https://doi.org/10.1029/2009GL041621>.
- , —, and —, 2012: Observed increases in Bering Strait oceanic fluxes from the Pacific to the Arctic from 2001 to 2011 and their impacts on the Arctic Ocean water column. *Geophys. Res. Lett.*, **39**, L24603, <https://doi.org/10.1029/2012GL054092>.
- , K. M. Stafford, and F. G. Prahl, 2015: A synthesis of year-round interdisciplinary mooring measurements in the Bering Strait (1990–2014) and the RUSALCA years (2004–2011). *Oceanology*, **28**, 46–67, <https://doi.org/10.5670/oceanog.2015.57>.
- Yamaguchi, M., and S. Maeda, 2020: Increase in the number of tropical cyclones approaching Tokyo since 1980. *J. Meteor. Soc. Japan*, **98**, 775–786, <https://doi.org/10.2151/jmsj.2020-039>.
- Yuan, L., and Z. Xiao, 2018: Impact of the Kuroshio Extension Oceanic Front on autumn and winter surface air temperatures over North America. *J. Ocean Univ. China*, **17**, 713–720, <https://doi.org/10.1007/s11802-018-3468-z>.
- Zhang, J., and D. A. Rothrock, 2001: A thickness and enthalpy distribution sea-ice model. *J. Phys. Oceanogr.*, **31**, 2986–3001, [https://doi.org/10.1175/1520-0485\(2001\)031<2986:ATAEDS>2.0.CO;2](https://doi.org/10.1175/1520-0485(2001)031<2986:ATAEDS>2.0.CO;2).
- , and —, 2003: Modeling global sea ice with a thickness and enthalpy distribution model in generalized curvilinear coordinates. *Mon. Wea. Rev.*, **131**, 845–861, [https://doi.org/10.1175/1520-0493\(2003\)131<0845:MGSIIWA>2.0.CO;2](https://doi.org/10.1175/1520-0493(2003)131<0845:MGSIIWA>2.0.CO;2).
- , R. Woodgate, and R. Moritz, 2010: Sea ice response to atmospheric and oceanic forcing in the Bering Sea. *J. Phys. Oceanogr.*, **40**, 1729–1747, <https://doi.org/10.1175/2010JPO4323.1>.
- Zwiers, F. W., and H. von Storch, 2004: On the role of statistics in climate research. *Int. J. Climatol.*, **24**, 665–680, <https://doi.org/10.1002/joc.1027>.